Since "real" life is possible only through knowledge, those who neglect learning and teaching are considered "dead", for we are created to learn and to communicate what we have learned to others. Truly valuable indeed are those who use their knowledge as a prism to perceive things and events, as a light to illuminate "space" to the darkest points, and to reach the most transcendent truths...

Fethullah Gulen

University of Alberta

Trapped Modes in the Plasmapause

by

Hava Turkakin

A thesis submitted to the Faculty of Graduate Studies and Research in partial fulfillment of the requirements for the degree of Master's of Science

Department of Physics

Edmonton, Alberta
Spring 2008

Library and Archives Canada

Published Heritage Branch

395 Wellington Street
Ottawa ON K1A 0N4
Canada

Bibliothèque et Archives Canada

Direction du Patrimoine de l'édition

395, rue Wellington
Ottawa ON K1A 0N4
Canada

Your file Votre référence
ISBN: 978-0-494-45900-3
Our file Notre référence
ISBN: 978-0-494-45900-3

NOTICE:
The author has granted a non-exclusive license allowing Library and Archives Canada to reproduce, publish, archive, preserve, conserve, communicate to the public by telecommunication or on the Internet, loan, distribute and sell theses worldwide, for commercial or non-commercial purposes, in microform, paper, electronic and/or any other formats.

The author retains copyright ownership and moral rights in this thesis. Neither the thesis nor substantial extracts from it may be printed or otherwise reproduced without the author's permission.

AVIS:
L'auteur a accordé une licence non exclusive permettant à la Bibliothèque et Archives Canada de reproduire, publier, archiver, sauvegarder, conserver, transmettre au public par télécommunication ou par l'Internet, prêter, distribuer et vendre des thèses partout dans le monde, à des fins commerciales ou autres, sur support microforme, papier, électronique et/ou autres formats.

L'auteur conserve la propriété du droit d'auteur et des droits moraux qui protège cette thèse. Ni la thèse ni des extraits substantiels de celle-ci ne doivent être imprimés ou autrement reproduits sans son autorisation.

In compliance with the Canadian Privacy Act some supporting forms may have been removed from this thesis.

While these forms may be included in the document page count, their removal does not represent any loss of content from the thesis.

Conformément à la loi canadienne sur la protection de la vie privée, quelques formulaires secondaires ont été enlevés de cette thèse.

Bien que ces formulaires aient inclus dans la pagination, il n'y aura aucun contenu manquant.

Canada

Abstract

The Earth's plasmasphere is a dense and cold region of the magnetosphere that is populated by the outflow of ionospheric plasma along mid- and low-latitude magnetic field lines. The plasmasphere is characterized by a sharp decrease in density at its boundary, the plasmapause, typically located between 2 and 6 Earth radii. The precise position of the plasmapause can vary considerably depending on the solar wind conditions and on the activity in the magnetosphere. As a result of this step-like density profile, combined with the monotonically increasing dipole magnetic field close to the Earth, compressional waves propagating outside the plasmapause can tunnel through and be trapped in a narrow layer that acts as a potential well. The wave equations in this well, in turn, can be described by the one-dimensional wave equation which is similar to the Schrödinger equation.

In this thesis, the spectrum and the spatial structure of these resonant localized modes is discussed for representative plasmasphere parameters. The data from SAMNET and IMAGE magnetometer arrays are used to infer representative density profiles in the plasmasphere. These data are then used to analyze the existence and properties of trapped compressional modes in the plasmapause.

To

My husband and my children who were always supportive, and to my mom who always believed in me

Preface

The Earth has a dipole magnetic field created by currents in its core. This field protects the Earth from the effects of the solar wind. When the solar wind reaches the Earth, it is deflected around it, forming a standing shock, the bow shock. The solar wind is slowed down at the bow shock and kinetic energy of the solar wind is transformed into thermal energy. The region between the bow shock and the region of the magnetosphere where field lines are closed (the magnetopause) is called magnetosheath. The plasma in Earth's magnetosphere consists mainly of ionized protons and electrons, with small concentrations of He^+, O^+, He^{++}. Moreover, the plasma in the magnetosphere is not evenly distributed, forming several distinct regions such as the radiation belts, the plasmasphere, the plasma sheet, and the magnetotail lobe.

The plasmasphere is a cold toroidal plasma region co-rotating with the Earth. It is the region of interest in this work. The plasmaspheric plasma originates mainly from the ionosphere. Its high density is due, in part, to the fact that the magnetic field lines in that region are closed. It is also a region where Earth's gravitational field is strong and dominates over the centrifugal force associated with co-rotation. This cold, dense plasma region is terminated at a sharp boundary called the plasmapause, after which there is a region of plasma with low density called plasmatrough. The sudden drop in density at the plasmapause leads to interesting dynamics in the plasmasphere and in the magnetosphere. For instance, reflection and transmission of the magnetohydrodynamic (MHD) waves in the magnetosphere are significantly affected by the presence of the plasmasphere and the plasmapause [4], and compressional MHD waves may be trapped or virtually trapped at the plasmapause due to the steep density drop in that region [1]. It is also suggested [1] that the possibility of these trapped modes could be the explanation of the low latitude Pi_2 pulsations which has the frequency range of 2-25 mHz.

Even though the possibility of the cavity or trapped modes in the plasmapause has been suggested, clear evidence for their existence has not yet been shown. In this thesis, using observed steep density profiles from three different geomagnetic storms, it is demonstrated that the compressional MHD waves can be trapped in the plasmapause. For the purpose of the analysis, profiles are taken at the times of magnetic disturbances because the steep density drops are mainly seen during these times.

There are four chapters in this thesis: In chapter one, a brief review of the Earth's magnetosphere, and the plasmasphere is presented. The possibility of the existence of the compressional MHD waves and trapped modes is explained. In chapter two, an

idealized problem is presented, which exhibits the essential features of resonant quasi-trapped modes in a well with tunneling losses. The problem was then solved analytically and numerically. The solution of the problem is compared with analytical solution, as a verification of the validity of the numerical approach. In chapter three, a set of equations was derived for compressional waves, in the plasmasphere, assuming a $1/R^3$ dependence for the magnetic field in that region. The resulting potential well was associated with the non-monotonicity in the Alfvén velocity. These equations were then solved using a one-dimensional box model of the magnetosphere. After the wave equation was derived, the solution was found again using a one dimensional central-difference code and a fourth order Runge-Kutta method. In this analysis three different data sets were used, corresponding to different solar wind conditions and magnetospheric disturbances. The corresponding density profiles were inferred from SAMNET and IMAGE magnetometer arrays [9]. All profiles showed evidence of the existence of the trapped or virtually trapped compressional modes. In both chapters, two and three, the quality factor, Q, which is an important parameter in trapped resonances was calculated numerically. It was found that for the peak values of Q (in the graphs as a function of real frequency), a clear spatial localization is observed in total energy at the plasmapause position, suggesting the possible existence of the trapped or virtually trapped compressional modes. Finally in chapter four the results are summarized and an outlook on possible future work is presented.

Acknowledgements

I would like to thank my supervisor, Richard Marchand, who was very helpful, and without whom this thesis would not have been possible. I owe thanks to Zoë C. Kale (Dent) for providing the measured data for my thesis. Additionally, I would like to thank my thesis committee members and friends.

Table of Contents

1 The Earth's Magnetosphere **1**
- 1.1 Introduction . . . 1
- 1.2 Coordinate System . . . 2
- 1.3 The Earth's Magnetosphere . . . 3
- 1.4 Plasmasphere and Plasmapause . . . 6
  - 1.4.1 Formation of the Plasmasphere and Plasmapause . . . 8
  - 1.4.2 Position of the Plasmapause . . . 11
  - 1.4.3 Density Profile . . . 14
  - 1.4.4 Waves Associated with the Plasmasphere and the Plasmapause . . . 17
  - 1.4.5 Trapped Compressional MHD Waves in the Plasmapause . . . 20

2 Ideal Case: Toy Problem **23**
- 2.1 Construction of the Wave Function . . . 24
  - 2.1.1 Continuous spectrum with an incoming wave of unit amplitude . . . 24
  - 2.1.2 Discrete spectrum and quality factor - analytic solution . . . 26
  - 2.1.3 Discrete spectrum and quality factor - numerical solution . . . 28

3 First Approximation: Box Model **33**
- 3.1 Construction of the Velocity Wave Function . . . 33
  - 3.1.1 Calculation of the energy density . . . 41
  - 3.1.2 Calculation of the effective potential . . . 43
- 3.2 Fitting a Function to a Plasmasphere Density Profile . . . 44
  - 3.2.1 The Alfvén velocity profile . . . 45
- 3.3 Numerical Solution . . . 46
- 3.4 Case Studies . . . 48
  - 3.4.1 Profile 1 . . . 48
  - 3.4.2 Profile 2 . . . 54
  - 3.4.3 Profile 3 . . . 58

4 Conclusion and Future Work **67**
- 4.1 Concluding Remarks . . . 67
- 4.2 Future Work . . . 68

Bibliography **70**

List of Tables

3.1 Data of Halloween 2003 49
3.2 Data of May 2001 58
3.3 Data of September 1998 63

List of Figures

1.1 Solar Wind Deflection 2
1.2 Dipole Coordinates 3
1.3 Regions of the Earth's Magnetosphere 4
1.4 Synopsis of Magnetospheric Currents 6
1.5 Earth's Plasmasphere 7
1.6 Depletion of the Plasmasphere 9
1.7 Equi-potential Contours of the Magnetosphere 12
1.8 Formation of the Plasmapause 13
1.9 Variations in the Plasmapause Position 15
1.10 Change in the Plasmapause Density Profiles in terms of the K_p Index . . 16
1.11 Changes in the Plasmapause Density Profiles in terms of the D_{st} Index . 18
1.12 Illustration of Wave-mechanics 22

2.1 Idealized Potential 24
2.2 Amplitude 27
2.3 Wave Function for High Q 29
2.4 Wave Function for Low Q 30
2.5 Frequency Spectrum and Q Factor; Analytical and Numerical Solutions . 32

3.1 Box Model 37
3.2 Box model Coordinates 38
3.3 Density Fit 45
3.4 Alfvén Velocity 46
3.5 Density Profile 1 50
3.6 Alfvén Velocity; Profile 1 51
3.7 Frequency Spectrum and Q factor; Profile 1,$k_y = 0$ 52
3.8 Effective Potential and Total Energy For High Q; Profile 1, $k_y = 0$ 53
3.9 Total Energy For Low Q; Profile 1, $k_y = 0$ 54
3.10 Potential and Energy For High and Low Q; Profile 1, $k_y = 0$ 55
3.11 Frequency Spectrum and Q Factor; Profile 1,$ky \neq 0$ 56
3.12 Effective Potential and Total Energy For Low Q; Profile 1, $k_y \neq 0$ 57
3.13 Density Profile 2 59
3.14 Alfvén Velocity; Profile 2 60
3.15 Frequency Spectrum and Q Factor; Profile 2, $k_y = 0$ 61

3.16 Effective Potential and Total Energy For High Q; Profile 2, $k_y = 0$ 61
3.17 Frequency Spectrum and Q Factor; Profile 2, $k_y \neq 0$ 62
3.18 Effective Potential and Total Energy For High Q; Profile 2, $k_y \neq 0$ 62
3.19 Density Profile 3 64
3.20 Alfvén Velocity; Profile 3 64
3.21 Frequency Spectrum and Q Factor; Profile 3, $k_y = 0$ 65
3.22 Frequency Spectrum and Q Factor; Profile 3, $k_y \neq 0$ 65
3.23 Effective Potential and Total Energy For High Q; Profile 3, $k_y = 0$ 66
3.24 Effective Potential and Total Energy For High Q; Profile 3, $k_y \neq 0$ 66

Chapter 1

The Earth's Magnetosphere

1.1 Introduction

Although most people are not aware of the existence of plasma, the fourth state of matter, a large fraction of our universe is in plasma state. Plasma is an ionized gas which is generally electrically neutral. In our solar system plasmas are abundant even in the neighborhood of the Earth. Indeed, above approximately 80 km of altitude, the atmosphere gradually turns into the ionosphere and the magnetosphere, and it has to be described in terms of the plasma physics.

The source of energy and plasma in the near Earth space environment is the solar wind and radiation. The solar wind is a highly conducting plasma released by the sun at supersonic speeds of $\sim$500 km/s into the interplanetary space. The solar wind is produced as a result of the expansion of the solar corona and consists of electrons and protons and a low percentage of helium and other minority ions. The Earth's magnetic field, approximately a dipole at distances $\sim 2R_E$ (Earth radii) [7], is an obstacle to the solar wind. The magnetic field of the Earth causes the solar wind to be deflected and leads to the formation of a cavity in the solar wind (see figure 1.1). The solar wind hits the Earth's magnetic field with supersonic speed and a bow shock wave is generated. At this point the plasma is slowed down and the kinetic energy of the particles is converted into thermal energy, forming the magnetosheath with hotter and denser plasma and with higher magnetic field strength compared to that in the solar wind [5]. The plasma in the magnetosheath cannot penetrate the terrestrial field lines. Therefore, there exists a boundary between two regions called the magnetopause, and a cavity is formed called the magnetosphere. In this chapter a brief overview of the principal components of Earth's magnetosphere is given. Trapped magnetohydrodynamic(MHD) waves are then

Figure 1.1: Artist rendition of the deflection of the solar wind around the magnetized planets and the cavity formation (from www.msfc.nasa.gov/NEWSROOM/news/photos)

introduced and a literature review of the subject is presented.

1.2 Coordinate System

Before reviewing the general structure of the Earth's magnetosphere, it is worth talking about its geometry. The Earth's magnetic field could be approximated as a tilted dipole. The Earth's dipole magnetic field can be represented using three parameters: L, λ, and ϕ (see figure 1.2), where λ is the magnetic latitude, L is called the McIlwain parameter, and ϕ is longitude, measured counter-clockwise looking from the north pole. The locus

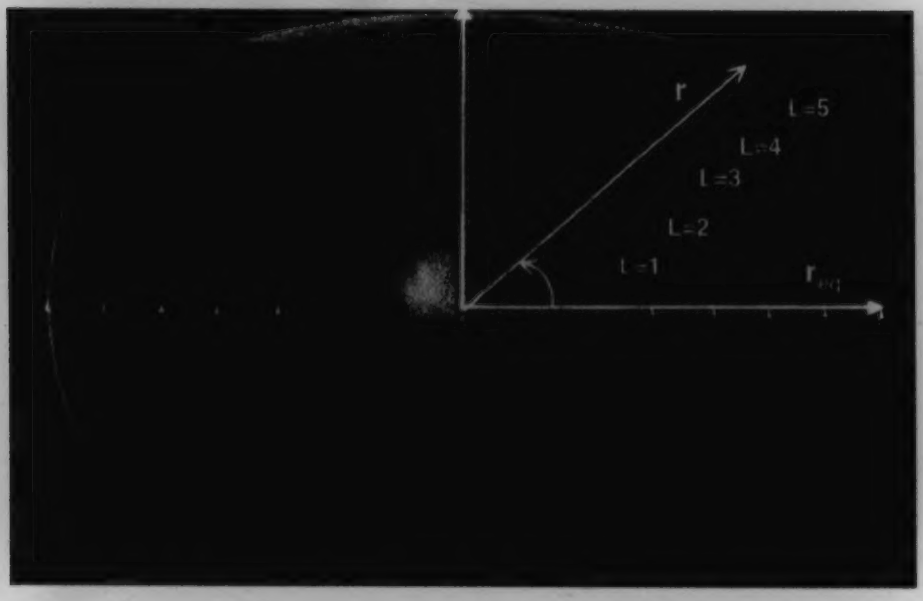

Figure 1.2: Coordinate system of the Earth's dipole magnetic field.

of a point on a particular field line is described as;

$$r = r_{eq} \cos^2 \lambda$$

$$r_{eq} = LR_E,$$

where r_{eq} is the equatorial distance of a field line, and R_E is the Earth's radius (R_E = 6378 km).

1.3 The Earth's Magnetosphere

As mentioned earlier, the Earth's magnetosphere is formed due to the interaction between the solar wind and the Earth's magnetic field. The solar wind is a highly conducting plasma and contains the solar magnetic field which is frozen in it as it moves with the solar wind flow. This frozen-in magnetic field, called the interplanetary magnetic field (IMF), is typically of the order of 5 nT. As a result of being frozen-in, or captive of the solar wind, the IMF cannot penetrate the terrestrial field lines. Thus a boundary called

magnetopause is formed separating the two regions. The cavity caused by the terrestrial field lines is called magnetosphere [5]. The magnetosphere has complicated dynamics and different plasma regions. The outer part of the terrestrial dipole magnetic field is

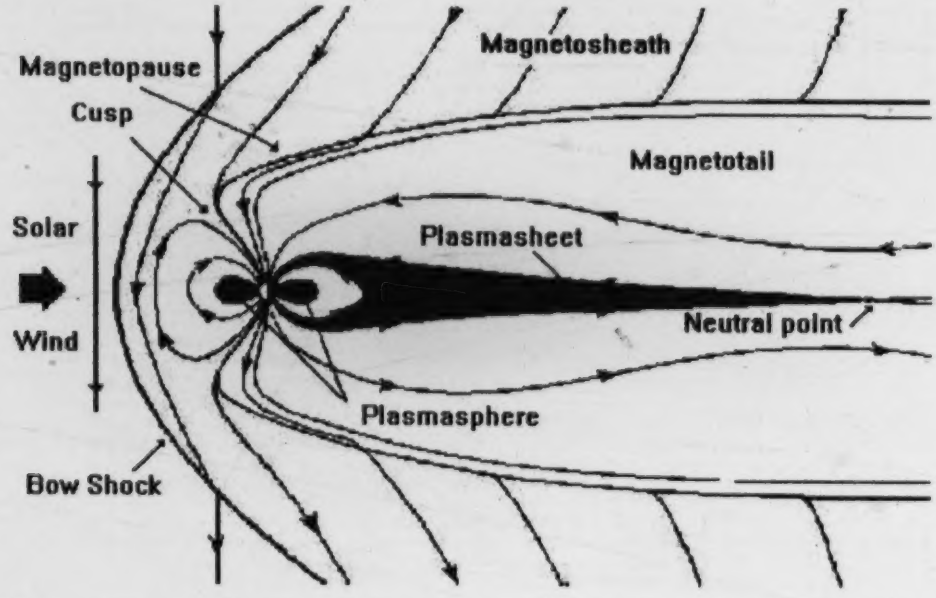

Figure 1.3: Plasma regions of the Earth's magnetosphere (from http://helios.gsfc.nasa.gov/magnet.html)

distorted by the solar wind kinetic pressure stretching the nightside and compressing the day-side. As a result a tail-like structure is formed on the night-side called magnetotail, extending beyond the lunar orbit. The day-side position of the magnetopause extends to approximately 8-10 R_E and the nightside position, to 100 R_E (1 R_E = 6378 km) [6]. The various parts of the magnetosphere plasma regions are illustrated in figure 1.3. The main components include the magnetotail, the plasma sheet, the magnetotail lobe, and the plasma sheet boundary layer. Closer to the Earth are the radiation belt, and the plasmasphere [7].

Most of the plasma in the magnetotail is contained in the plasma sheet, at $\sim$10 R_E in the tail midplane [5]. The plasma sheet consists of hot particles with particle densities of $\sim 0.1 - 1\ cm^{-3}$ [7]. The plasma sheet is populated mainly by solar wind particles during quiet times, and particles originating from the ionosphere during active times.

The plasma sheet boundary layer, generally observed as a transition region between magnetotail lobes and the hot plasma sheet, is the distant part of the plasma sheet in which the ions flow velocity is high with densities of order $\sim$0.1 cm^{-3}. The magnetotail lobe is the outer part of the magnetotail with low density plasma; lower than 0.1 cm^{-3}. The ions in the tail lobe are believed to be of ionospheric origin [7]. The radiation belts, also called Van Allen belts, are structures that lie between 2-6 R_E with the energetic particles oscillating between two hemispheres. These particles drift azimuthally around the earth due to the magnetic field gradient, thus forming the ring current. The number density and the energy density of the particles are more intense near the equatorial plane and less intense at low latitude since they interact with the neutral atmosphere and become lost. There exist two radiation belts, namely an inner and an outer one. The characteristic electron density in the radiation belts is $\sim 1\ cm^{-3}$, the temperature is $\sim 5 \times 10^7$ K, and the magnetic field strength varies between $\sim$100 and 1000 nT [5]. The plasmasphere which will be discussed in more detail in the following section coexists in approximately the same region as the radiation belts [7].

The ionosphere is also an important region forming the inner edge of the magnetosphere. It is formed by the photoionization of high altitude atmospheric molecules by UV and X-ray radiation from the sun. At high latitudes, it is also produced by the solar wind impinging on the Earth and ionizing part of the neutral atmosphere. A typical electron density in the ionosphere is $\sim 10^5\ cm^{-3}$ and temperatures are of order $\sim 10^3 K$ and the magnetic field strength is of order $\sim 10^4$ nT. The ionosphere merges into the plasmasphere at low and mid-latitudes.

The plasma in the magnetosphere can also sustain currents that feed back and affect the shape of the magnetosphere. Electrons and ions move in different directions producing electric currents which affects the dynamics of the magnetosphere significantly by transporting charge, mass, momentum and energy, and producing magnetic fields. For instance, the magnetopause current, the current flowing across the magnetopause surface, causes the compression of the terrestrial field lines on the day-side magnetosphere, and the tail-like shape of the night-side magnetosphere is due to the tail current (see figure 1.4). In figure 1.4, the ring current which is caused by particles in the Van Allen belts is also seen. The ring current flows around the Earth in the westward direction and it affects the inner configuration of the magnetosphere. Although electrons drift around the Earth eastward they do not have a significant effect on the net westward current, due to their relatively low mass, compared to ion masses. There also exist field aligned currents mainly formed by the electrons which, have strong effects on the exchange of energy and momentum different currents regions. At altitudes of 100-150 km, some cur-

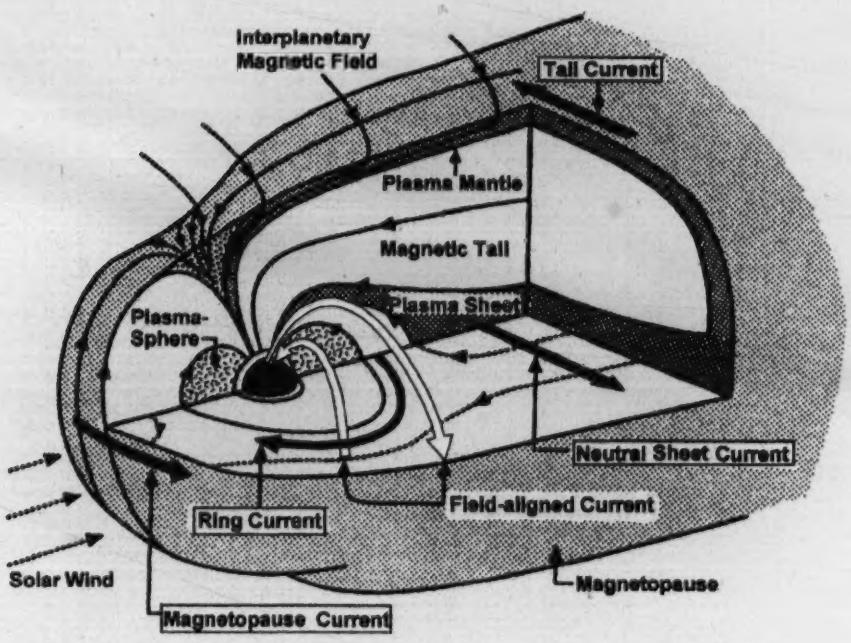

Figure 1.4: Synopsis of the magnetospheric currents (from www.ngdc.gov/seg/geomag)

rents exist in the conducting layers of the ionosphere such as the auroral electrojets, and the equatorial electrojet [5].

1.4 Plasmasphere and Plasmapause

The plasmasphere was discovered through whistler waves, which are very low frequency waves generated by lightning, and which which propagate along the lines of force of the Earth's magnetic field [8]. The observation of the whistler waves showed that there is a region of cold plasma particles, mainly protons and a small fraction of H^+ and He^+ [11], with high densities $\sim 10^3\ cm^{-3}$ and energies $\sim 1-2eV$. O^+ is also an observed ion species enhanced especially during the recovery time, following high geomagnetic activity periods [9]. Two simultaneous studies by K.I. Gringauz using satellite measurements and

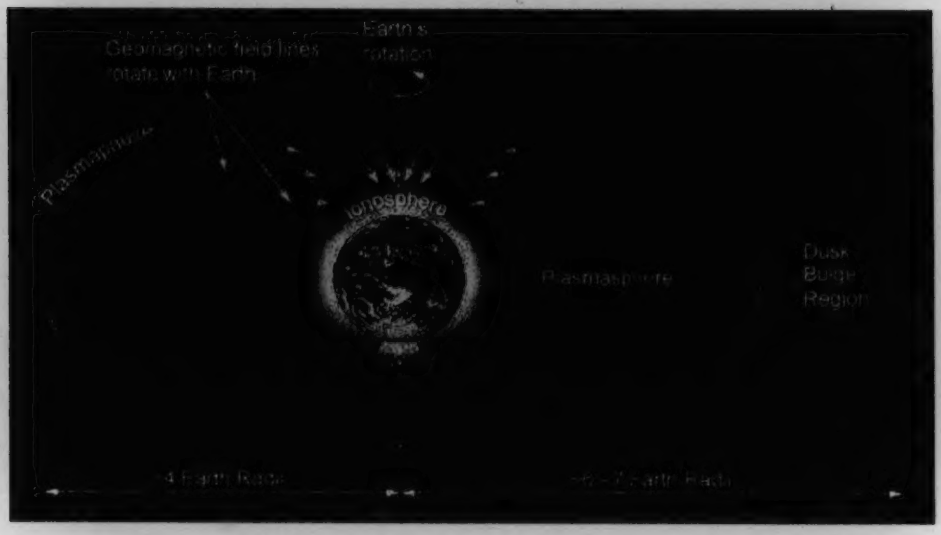

Figure 1.5: Schematic illustration of the Earth's plasmasphere (from www.windows.ucar.edu/tour/link=/glossary/plasmasphere.html)

D.L.Carpenter using ground-based measurement have showed that this region of dense and cold plasma is frequently terminated by a sharp boundary called plasmapause [7]. The position of the plasmapause is typically between 3 and 5 R_E. It is closer to Earth during high geomagnetic activities and extends up to 6-7 R_E during low activity times. It has a bulge formation due to solar wind disturbances (see figure 1.5). Although from the data collected with the ISEE satellite the plasmasphere is observed to be approximately circular, bulges on the dusk sector are also observed mostly at earlier local times during high solar wind disturbances and at later local times during quiet times [11].

Just outside of the plasmapause, there is a low density plasma region called the plasmatrough which is populated by plasma particles with densities of order $1 - 10$ cm^{-3}.

Around the Earth there is an approximate co-rotation flow of the plasma and, further from the Earth there is a convective flow towards the sun. The co-rotating plasma forms the plasmasphere. As a result of heating from solar UV radiation, and energization from electric fields induced by magnetospheric activity, plasma particles from the ionosphere escape along the magnetic field lines to form the plasmasphere [36].

The plasmasphere and the plasmapuse are highly dynamic regions and they are af-

fected by the solar wind interactions with the Earth. During geomagnetic storms the outer region of the plasmasphere can be transported outward and sunward to the magnetopause (see figure 1.6). During the onset of geomagnetic disturbances, the night-side plasmapause shows an inward motion with the distance at a velocity of approximately 0.5 R_E per hour, and a stripping of plasma towards the sun [11]. This erosion is related to the turning of the interplanetary magnetic field (IMF) southward, and the instantaneous rotation velocity of the plasmapause is enhanced by the strength of the IMF [11]. It has been suggested that the sudden density drop at the plasmapause is due to this enhancement of the velocity [8].

The plasmaspheric bulge also changes its shape by moving noon-ward and decreasing its width at high geomagnetic disturbances [10]. During high magnetospheric activity, the strong convection ablates the outer plasmasphere flux tubes, thus causing the plasmapause to get closer to the Earth [7]. Once magnetospheric activity ceases the plasmasphere depleted flux tubes are gradually refilled from the ionosphere [9]. Ion temperatures are higher in the inner plasmasphere than those of the plasmapause [7].

1.4.1 Formation of the Plasmasphere and Plasmapause

Of the different theories of the formation of the plasmapause and plasmasphere, the simplest one is that it is formed by the large-scale electric field interactions. In this model, the terrestrial magnetic field is assumed to be a centred dipole and the magnetosphere is in steady state. The plasma in the dipole magnetic field is assumed to be cold and the solar wind velocity to be constant [12].

The cold plasma and the field lines in the magnetosphere are influenced by two major energy sources, namely the solar wind kinetic energy in the outer magnetosphere and daily rotation of the Earth in the inner magnetosphere [5]. As stated before, the field lines of the Earth are stretched by the solar wind flow down the magnetotail. Plasma in the magnetosphere is transported together with the magnetic field lines since it is frozen-in with them. Basically, the magnetic field lines are connected to the IMF on the day-side. They are swept down to the magnetotail and reconnected on the night-side. After this reconnection these field lines move back to their dipole position completing the cycle by sunward flow of plasma in the inner magnetosphere. The simultaneous drift of the plasma with the field lines is referred to as convection which, in turn, is associated with a convection electric field [5]. Reconnection occurs when the IMF is southward, as previously stated. The solar wind and IMF generates a convection electric field which is

Figure 1.6: Depletion of the plasmasphere during high geomagnetic activity is shown in an ultraviolet image, taken by NASA's IMAGE satellite. The bulge of the plasmasphere towards the sun is clearly seen. The photo is taken by the IMAGE satellite. The bulge had been postulated before, but the picture above was the first ever taken made of its actual shape. IMAGE remains in operation to this date and it continues to study how geomagnetic storms effect the Earth's magnetosphere (from http://apod.nasa.gov/apod/image/0101/,Jan,2001)

directed from dawn to dusk as described by,

$$\mathbf{E}_{Cn} = -\mathbf{V}_{sw} \times \mathbf{B}_{IMF},$$

where $\mathbf{V}_{sw}$ is the solar wind velocity and $\mathbf{B}_{IMF}$ is the interplanetary magnetic field strength.

There is also a co-rotation electric field caused by the rotation of the Earth, which is defined as

$$\mathbf{E}_{Cr} = -\mathbf{V}_{Cr} \times \mathbf{B}_{dipole},$$

where $\mathbf{V}_{Cr}$ is the Earth's co-rotational velocity and $\mathbf{B}_{dipole}$ is the dipole magnetic field of the Earth. The plasmasphere is formed due to large scale interactions of the above electric fields. If convection is stable then $\partial \mathbf{B}/\partial t = 0$, and hence $\nabla \times \mathbf{E} = 0$. Thus, the convection electric field can be expressed as

$$\mathbf{E}_{Cn} = -\nabla \Phi_{Cn},$$

where Φ_{Cn} is the convection potential defined to be

$$\Phi_{Cn} = -\mathbf{E}_{Cn} L R_E \sin(\phi)$$

in the equatorial plane, where ϕ is azimuthal angle, and LR_E is the radial distance.

On the other hand, the co-rotation electric field could be written as

$$\mathbf{E}_{Cr} = -(\boldsymbol{\omega} \times \mathbf{r}) \times \mathbf{B}_{dipole},$$

where $\omega = 7.29 \times 10^{-5} rd/s$ is the angular velocity of the rotation of the Earth and $\mathbf{r}$ is the radial distance from the Earth's centre. On the equatorial plane

$$E_{Cr} = \frac{\omega B_E R_E}{L^2}.$$

where $B_E = 3.11 \times 10^{-3}$ T is the equatorial magnetic field on the surface of the Earth.

As can be seen from the above equation the co-rotation electric field decreases as $1/L^2$ and, in the equatorial plane, it is directed radially inward. The equatorial plane electric potential can also be calculated using the relation $\mathbf{E}_{Cr} = -\nabla \Phi_{Cr}$, which gives

$$\Phi_{Cr} = -\frac{\omega B_E R_E^2}{L}.$$

The streamlines of the convection potential are open straight lines directed towards the sun and the co-rotational equi-potentials are closed circles (see figure 1.7). Inside the magnetosphere the motion of the plasma is affected by both the convection and the co-rotation electric field. The total electric potential in the equatorial plane is

$$\begin{aligned} \Phi_t &= \Phi_{Cn} + \Phi_{Cr} \\ &= E_{Cn} L R_E \sin(\phi) - \frac{\omega_E B_E R_E^2}{L}. \end{aligned}$$

As can be seen from the above total electric potential, close to the Earth co-rotation dominates and the plasma co-rotates with the Earth. As a result, the equi-potential contours are closed circles. Farther away, on the other hand, equi-potential contours are open and convection dominates. As mentioned before, the co-rotation electric field points radially inward in the equatorial plane and the convection electric field points from dawn to dusk. Two classes of streamlines cross each other on one contour that supports zero electric field at 1800 local time and separates the closed and open streamlines (see figure 1.7). This equi-potential contour is the position where the plasmapause is formed. Within the plasmapause, plasma is frozen-in and co-rotates with the Earth forming the plasmasphere [12]. Outside the plasmapause the streamlines goes to the day-side magnetopause and day-side reconnection causes the flux tubes to open and plasma is then lost to the solar wind.

In addition to the convection and co-rotation electric field theory, it is also proposed that the plasmapause is the stripped part of the post-midnight sector due to the magnetic flux tubes interchange motion driven by the Roche-limit surface. The Roche-limit is the surface where the gravitational and centrifugal forces balance each other in the local magnetic field direction [18]. Figure 1.8 illustrates the plasmapause position following this viewpoint. At $L \geq 4.5$ the centrifugal (or inertial) forces are dominant, the plasmasphere is peeled off and the plasmapause is formed. The plasmasphere will be bounded by a surface which almost matches the equi-potential that is tangent to the Roche-limit surface at its deepest penetration point if the electric field distribution does not change for around 24 hours or more [18]. In this model the position of the plasmapause is described as the minimum radial distance of the Roche-limit surface.

1.4.2 Position of the Plasmapause

The separatrix at which the convection and co-rotation streamlines cross each other is called the Alfvén layer. The Earth rotates eastward, therefore the sunward convection flow and the co-rotation flow are in the same direction on the dawn side and in the

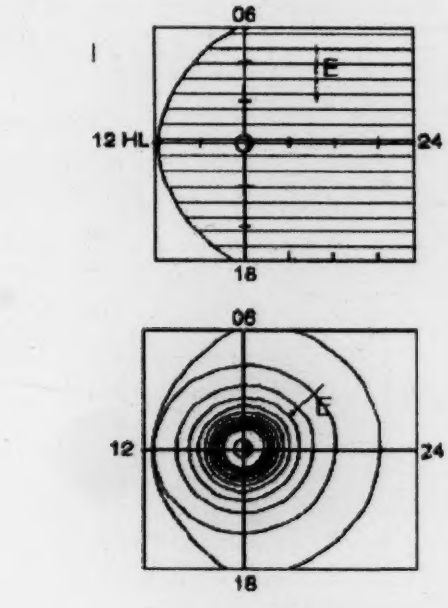

(a)

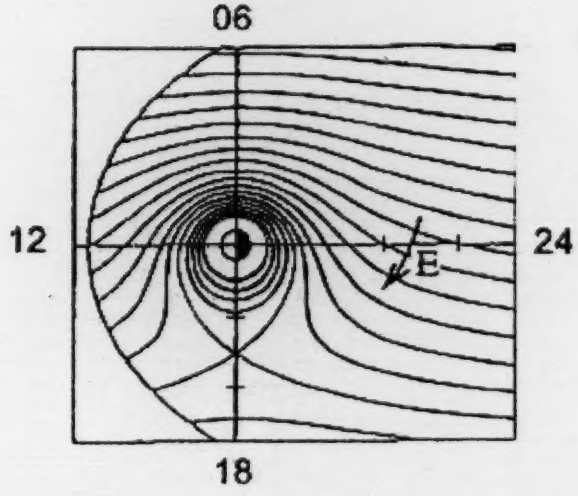

(b)

Figure 1.7: Electric equi-potential lines in the equatorial plane. Small figures on the top and in the middle, figure (a) shows convection and co-rotation lines respectively and the direction of the corresponding electric fields. Figure (b) illustrates the superposition of the total equi-potential lines and particle drift motion with the red line representing intersection of the closed and open equi-potential lines.The sun is located on the left [15].

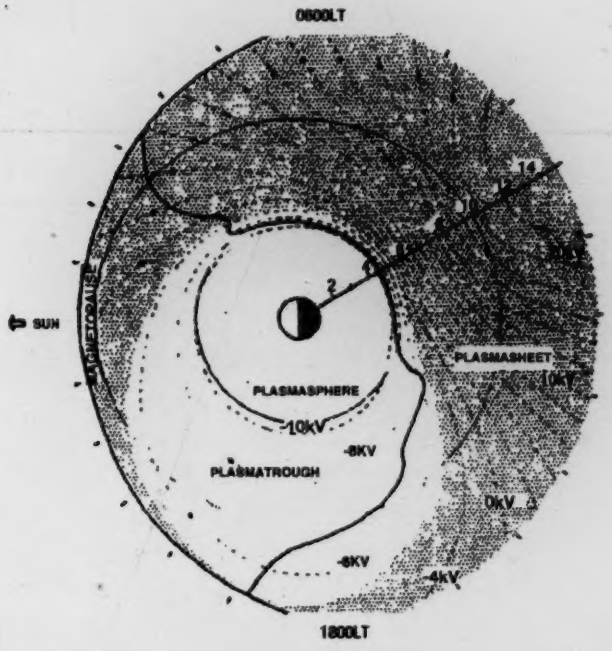

Figure 1.8: Illustration of the plasmapause formation with the effect of the balance between the gravitational and centrifugal forces at the Roche limit surface. The solid line is the equatorial section of the Roche limit surface, the dashed lines are the equi-potential lines and the boundary of the outer shaded region is the last closed equi-potential line; that is, the Alfvén layer [18].

opposite direction on the dusk side. This configuration produces a lower drift on the dusk side and a higher drift on the dawn side, causing the Alfvén layer to be closer to Earth on the dawn and farther on the dusk regions (see figure 1.9) [13]. At the point on the dusk side of the Alfvén layer where the plasmasphere has a bulge, the eastward co-rotation and westward convection cancel each other. Thus at this point, referred to as the stagnation point, the plasma flow velocities vanish. The distance of the stagnation point from the Earth could be found by using the relation $\Phi_{Cn} = \Phi_{Cr}$ and $\sin(\phi) = 1$, which gives

$$L_{Sp} = \left(\frac{\omega_E B_E R_E}{E_{Cn}}\right)^{\frac{1}{2}}$$

showing clearly that the distance of the stagnation point is inversely proportional to the convection electric field.

The above definition of the plasmapause as the position of the last closed equipotential assumes that the magnetospheric electric field distribution is stationary in time. The solar wind, however, is hardly ever stationary. As a result, the convection electric field is also usually changes in time. The general enhancement of solar wind flux and the fluctuations in the IMF affects the convection electric field which determines the position of the Alfvén layer, and thus of the plasmapause, and cause them to change continually. Once the convection electric field becomes stronger, during geomagnetic storms, then the plasma in the outer plasmasphere will flow along the streamlines of this enhanced electric field and will be lost to the magnetosphere. This process causes the position of the plasmapause to change continually [8]. The plasma that is parted from the plasmasphere is sometimes transported to the magnetotail and eventually into the plasma sheet with a small probability of escape into the solar wind. At the end, the convection electric field weakens and 10-30% of the swept plasma becomes trapped between the plasmasphere and the magnetopause. After several days of recovery following a storm, some of the eroded plasma becomes tied to the plasmasphere and begins to rotate with the Earth. The plasmasphere is refilled by ionospheric plasma outflow. Figure 1.9 illustrates the evolution of the Alfvén layer after an enhancement of the convection electric field. The fastest changes at the plasmapause position arise near the dusk sector. After 6-10 hours from the disturbance, the plasmapause moves to a new equilibrium position closer to the Earth [13]. The erosion could last from hours to tens of hours, after which follows the refilling of the plasmasphere which requires several days, and the thermalization of the counter-streaming plasmas. These phenomena are still the subject of active research [14]. Statistical and case studies of the events that follow a magnetic disturbance have shown that the refilling of the plasmasphere generally takes place on a long time scale [16].

At the extreme of magnetic activity, geomagnetic storms cause the location of the plasmapause to vary significantly, with an outer boundary as close as 2.5 R_E during high activity times, compared to $\sim 6 - 7R_E$ during quiet times.

1.4.3 Density Profile

The sharp density drop at the plasmapause is the result of the solar wind disturbances. The plasmapause position moves closer to the Earth just after a geomagnetic storm. As a result of this, a sharp density decline is observed at the plasmapause. The density in the quiet plasmasphere falls off with L more slowly [8]. Figure 1.10 clearly shows the

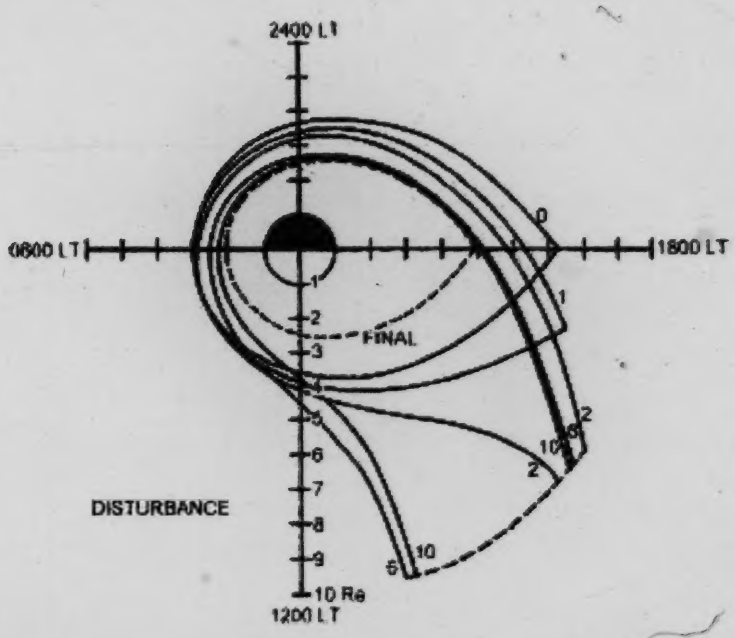

Figure 1.9: Computed plasmapause position after an enhanced convection electric field. The labels show the different positions of the plasmapause at different times of the enhancement. 1.,2,.....10 shows the computed positions after corresponding hours of the enhancements and 0 represents the Alfvén layer. The dotted line labeled 'FINAL' shows the steady-state plasmapause position after a long period of time [13].

effect of the solar wind disturbances on the density profile of the plasmapause. In figure 1.10 the solar wind disturbance strength is expressed in terms of the K_p index. This index is a measure of the mean maximum fluctuations (relative to the average on a quiet day) in the horizontal component of the Earth's magnetic field over a three-hour interval, obtained from a number of magnetometer stations around the world [34]. During strong solar wind disturbances the fluctuations in the geomagnetic field components are larger, thus the K_p index is larger and the plasmapause density drop is sharper. For instance, no sharp boundary was observed when the solar wind was quiet, $K_p < 1^+$. When the solar wind was active, however, the plasmasphere boundary is sharp and well defined. These points are illustrated in figure 1.10, where the position of the plasmapause is seen to be closer to the Earth as the disturbance gets stronger. It is inferred from whistler

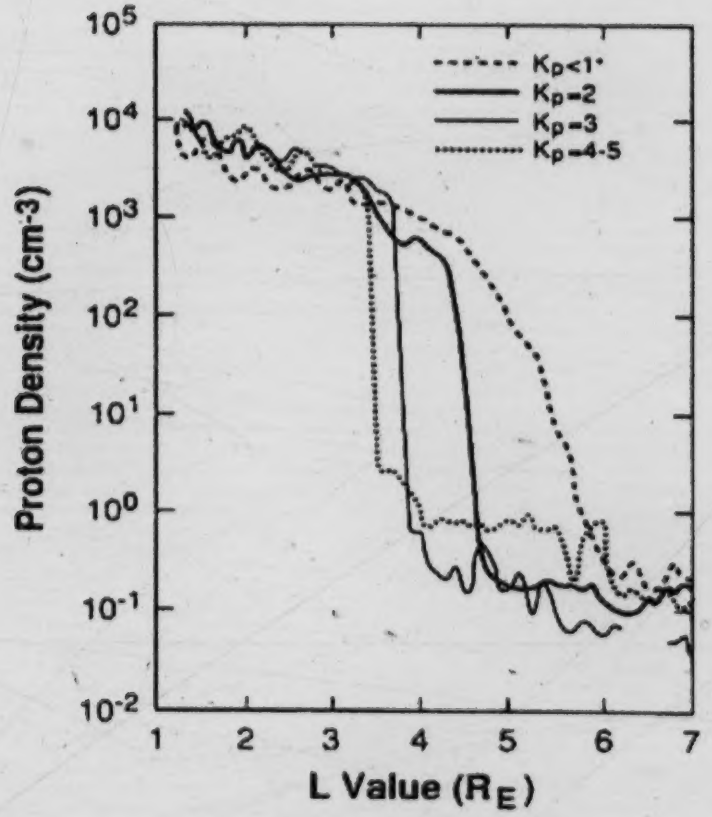

Figure 1.10: Density profile of the plasmasphere at different K_p indices. High K_p index represent a higher level of magnetic activity; that is, the solar wind disturbances strength(http://www.new.ss.ncu.edu.tw/ lyu/).

wave data that the reduction in the main plasmasphere size at the time of disturbances is generally accompanied by a decrease in the electron density by a factor of $\sim 1.2-3$ in the outside of the eroded parts. The whistler waves are caused by the lightning discharges and the name whistler comes from the nature of their dispersion relation [7].

The plasmapause density gradient can vary azimuthally, and can be sharp or shallow depending on the conditions [9]. The density discontinuity is mostly seen on electron and H^+ density profiles; heavy ions do not contribute much and their effect is mostly neglected. The density profile of the plasmapause can be very sharp at most local times [17]. The scale of the density drop at the plasmapause varies but it could be approximated as $0.1R_E$ on the nightside and $0.2R_E$ on the day-side. In this thesis the electron number density is used to characterize the steep decline at the plasmapause. Once the electron number density is known, assuming a pure hydrogen plasma for simplicity, the plasma mass density can be inferred [9]. Figure 1.11 illustrates the change in the electron number density profile with the geomagnetic activity measured by using the D_{st} index. D_{st} is a disturbance storm time index measuring the horizontal component of the Earth's magnetic field which is inversely proportional to the energy content of the ring current which increases during geomagnetic storms [14]. Thus the D_{st} index decreases during the geomagnetic storms.

In quiet times the plasmapause moves further away from the Earth and does not have a steep density decline anymore, as pointed out before. The sharp decline of the density profile at the plasmapause and the resulting non monotonic profile in the Alfvén velocity are responsible for the appearance of an effective potential well capable of trapping compressional waves. This constitutes the main interest of this project.

1.4.4 Waves Associated with the Plasmasphere and the Plasmapause

Interesting incidences of wave phenomena, believed to be associated with the abrupt density decline at the plasmapause, have been observed or theorized at or in the vicinity of the plasmapause. The steep density drop could be a source of boundary waves at the plasmapause; a unique kind of whistler wave mode is observed just beyond the steep decline of the plasmapause density profile. This region is also suggested to be the region for kilometric continuum radiation [19]. Non-monotonic change of the Alfvén velocity due to steep density drop acts as a resonator affecting the structure of the hydromagnetic waves in the inner magnetosphere [20]. During geomagnetic disturbances, energetic particles are transported to the plasmapause region by convection flow and they cause ion cyclotron instabilities with wavelengths of the order $10^2 - 10^3 m$ [21]. The two MHD modes, compressional and shear modes, are decoupled in a cold uniform plasma, but

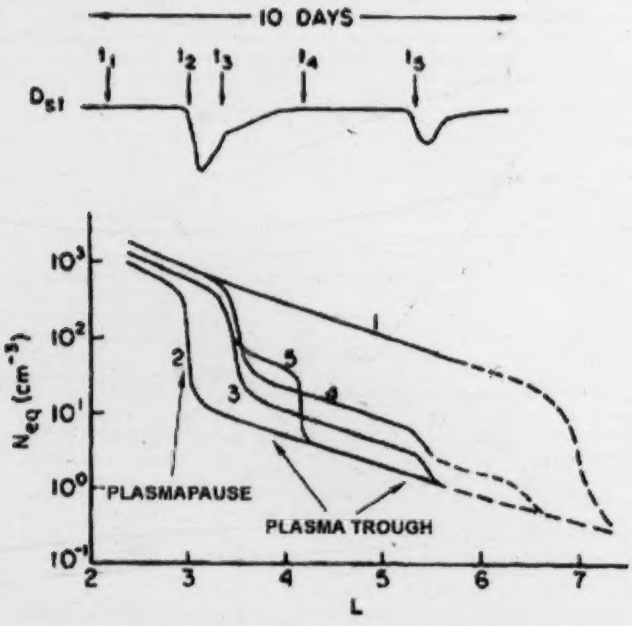

Figure 1.11: Electron number density profile during two active geomagnetic storms of 10 days period. The D_st index is plotted for the time interval with the drops indicating geomagnetic storms. A steep drop is seen with the onset of storm(line 2 corresponding t_2), after the quieting, the plasmasphere refills and density in the eroded region increases. A second storm interrupts the refilling process and a steep drop is seen again at L=4.2 (line 5) [14]

they are coupled in the non-uniform magnetosphere. The shear modes, also called Alfvén waves, and two types of the compressional wave modes, the fast and slow modes, are possible. The irregularity at the plasmapause is a crucial issue in wave coupling in the magnetosphere. It is also proposed that there is an abrupt increase in the frequency of the upper hybrid resonance band at the plasmapause [27].

Finally, the plasmasphere and plasmapause are suggested to be effective in mode trapping in the magnetosphere. MHD wave trapping is also suggested in between the inner plasmapause boundary and outer magnetopause boundary. The reflection and the transmission of the MHD waves is significantly affected by the presence of the plasmapause [4]. It is also discussed in [4] that the Alfvén speed barrier caused by the steep

decline in density at the plasmapause plays an important role on the reflection and transmission of the compressional waves in the inner magnetosphere. Since the Alfvén speed crest represents the boundary between the outer magnetosphere and the plasmasphere, it has significant effects on wave phenomena. It is also proposed that wave trapping in the cavity between high density magnetopause and plasmapause regions generates the terrestrial continuum radiation which is observed in the plasmatrough region with frequencies higher than the local plasma frequency [26]. Continuum radiation is trapped in the magnetospheric cavity and dispersed uniformly due to repeated reflections at the cavity walls. Observations showed evidence of the standing compressional MHD modes bouncing to and fro between the magnetopause and the plasmapause. The sudden density drop causes the oscillation frequency, which is inversely proportional to the square-root of the density, to peak just outside the plasmapause [22].

ULF(Ultra Low Frequency) pulsations are fluctuations of the Earth's surface magnetic field [5]. They have two classification types: continuous(P_c1-5) and irregular(P_i1-2) [8][5]. P_c pulsations have periods in the range from several minutes to hours and wavelengths of several R_E, and they can be observed over a large latitudinal and longitudinal range [5]. There are two possible explanation of the generation of the P_c pulsation; they are generated by the surface waves that are a result of the Kelvin-Helmholtz instability caused by the solar wind flow around the magnetopause, or compressional waves entering the magnetosphere at its nose [5]. P_i pulsations have shorter periods and are more localized. They are thought to be associated with geomagnetic storms [5]. There also exist unexplained low and mid-latitude pulsations for which different possibilities of the generation has been suggested. With the combination of data and observation it has been suggested that the damped sinusoidal oscillations observed at mid-latitudes can be related to an MHD surface eigenmode excited at the sharp plasmapause density gradient [23][24]. The possibility of the plasmasphere acting as a resonant cavity for ULF waves has been explored [28], where it was concluded that plasmaspheric cavity resonance periods would be the most likely mechanism for the mid-latitude P_i2 pulsation. However, the existence of the cavity modes at the plasmapause has not been proven thus far. Surface waves is another possibility that is proposed for the cause of the low latitude ULF pulsation of P_c3-5 [23][30]. However, the possibility of surface waves was ruled out later on by several studies [28][2] where more emphasis was given to the possibility of cavity or waveguide modes [2]. Other papers were written in support of surface waves possibilities against trapped modes [22][31][32] . In the present thesis, the suggestions that cavity modes can exist at the plasmapause is supported and shown numerically with the calculation of the total energy and dispersion relation of the compressional MHD modes.

1.4.5 Trapped Compressional MHD Waves in the Plasmapause

Compressional MHD waves can convey energy across the magnetic field lines, thus they play a crucial role in ULF wave properties [3]. The behavior of the compressional MHD waves in the inhomogeneous magnetosphere has been given much attention in the past ([4][2][3][29][1]). In order to conceptualize compressional MHD modes an analogy is now presented between these waves and quantum mechanics. The similarity between the MHD wave equation and the Schrödinger equation is quite useful to grasp the idea of compressional MHD modes and their trapping or virtual trapping in the plasmapause. As is well known in quantum mechanics, if a potential barrier is present, waves can be trapped, virtually trapped, they can tunnel or scatter, depending on the wave and the potential barrier properties (see figure 1.12). In situations where the potential well has a structure such as illustrated in figure 1.12a, it is found that wave energy can be confined spatially in the region of the potential well. The corresponding trapped modes would be localized spatially in the region of potential through. In the situation illustrated in figure 1.12b, on the other hand, a wave coming from outside the region of potential crest would be scattered away from it. In figures 1.12c and 1.12d it is possible to have virtually trapped resonances depending on the frequency of the waves and the shape of the potential well. Waves with relatively low frequencies would be quasi-trapped modes. The waves with higher frequencies are no longer trapped forming virtual scattering resonances [3]. It can be seen that the density characteristics at the plasmapause leads to a profile in the Alfvén speed across the magnetosphere that corresponds to figures 1.12c and 1.12d, with the crest corresponding the region of the sharp density drop. It therefore follows that trapped or quasi-trapped modes might exist in the region of this Alfvén speed valleys.

Let us now make the analogy between compressional waves and the Schrödinger equation more precise [3]. The Schrödinger equation for a one dimensional potential barrier can be written as;

$$i\hbar\frac{\partial\psi(\mathbf{x},t)}{\partial t} = \left(-\frac{\hbar^2\nabla^2}{2m} + V(x)\right)\psi(\mathbf{x},t),$$

where $V(x)$ is the potential barrier, $\hbar$ is the Plank's constant, and $\psi(\mathbf{x},t)$ is the wave function. If it is assumed that the wave function, $\psi(\mathbf{x},t)$, is proportional to $e^{i(k_y y + k_z z - E/\hbar t)}$, the above equation turns into

$$\frac{d^2\psi}{dx^2} + \frac{2m}{\hbar^2}\left(E_n - V(x)\right)\psi = 0.$$

where $E_n = E - \frac{\hbar^2}{2m}\left(k_y^2 + k_z^2\right)$ is the effective energy. Arranging the above equation,

$$\left(\frac{d^2}{dx^2} + K_x^2(x)\right)\psi = 0, \tag{1.1}$$

is obtained, where $K_x^2 = \frac{2m}{\hbar^2}\left(E_n - V\right)$ is a function of the effective energy, and of the potential, $V(x)$.

Similarly, the MHD wave equation, for spatially uniform wave, for electric field components is

$$\nabla^2 \mathbf{E}_\perp - \frac{1}{V_A^2}\frac{\partial^2 \mathbf{E}_\perp}{\partial t^2} = 0$$

where V_A is the Alfvén speed and $E_\perp$ is the transverse electric field component. Again, for the purpose of making the analogy, the wave is assumed to be of the form $E(x)e^{i(k_y y + k_z z - \omega t)}$ and the constant Alfvén speed is formally replaced by $V_A(x)$ with x, y and z representing the radial, azimuthal and north-south directions respectively, the above equation becomes

$$\frac{d^2E}{dx^2} + \left(\frac{\omega^2}{V_A^2(x)} - k_y^2 - k_z^2\right)E = 0.$$

This equation can now be written as

$$\left(\frac{d^2}{dx^2} + k_x^2(x)\right)E = 0. \tag{1.2}$$

where $k_x^2 = \frac{\omega^2}{V_A^2} - k_y^2 - k_z^2$. In the following, only perturbations corresponding to compressional waves propagating across magnetic field lines are considered.

From the general properties of second order ordinary differential equations, it is clear that the solution to equation 1.1 is oscillatory when $K_x^2 > 0$, and that the solution to equation 1.2 will also be oscillatory when $k_x^2 > 0$. More specifically, for these two equations, the condition for having an oscillatory solution corresponds to $E_n > V(x)$ for equation 1.1, and $\omega > V_A(x)\sqrt{k_y^2 + k_z^2}$ for equation 1.2. The waves become evanescent when $K_x^2 < 0$ and $k_x^2 < 0$. Therefore, E_n and $V(x)$ in the Schrödinger equation are analogous to ω and $V_A(x)$ in the MHD wave equation respectively. Hence, the Alfvén velocity valley produced by the plasmapause density drop is mathematically analogous to the effective potentials shown in figures 1.12. Looking at the equation of the Alfvén speed, $V_A(x) = \frac{B_0(x)}{\sqrt{\rho_0(x)\mu_0}}$, a profile similar to figures 1.12c and 1.12d would be expected which would support quasi trapped resonances.

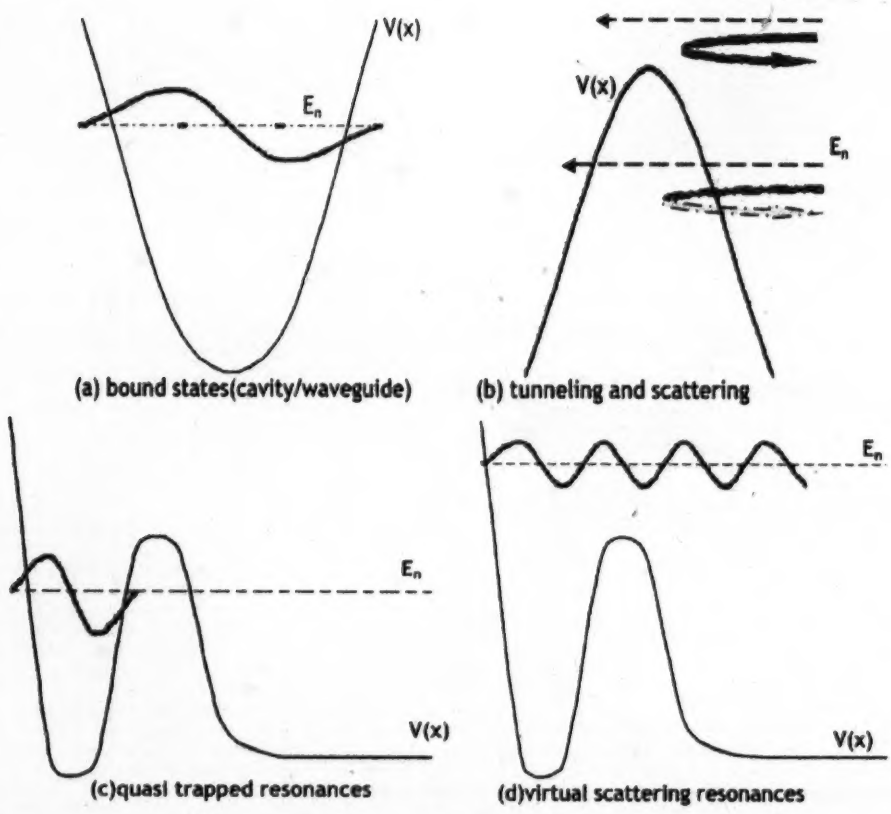

Figure 1.12: Illustrations of several possible potentials in wave mechanics. The energy E_n and potential $V(x)$ are analogous to the frequency, ω, and the Alfvén speed, V_A, respectively for compressional waves described in the MHD approximation.

Chapter 2

Ideal Case: Toy Problem

In this chapter, the problem is idealized by using a fictitious potential well that supports the existence of quasi-trapped modes, as introduced in the previous chapter. For simplicity, a step function is assumed as the potential barrier, as illustrated in figure 2.1. This constitutes an idealization of the compressional wave problem of interest here. As a starting point, the mode trapping is addressed by solving the wave equations assuming an incoming wave from the right, with unit amplitude. By considering the amplitude of the solution in the potential well (region 1 in figure 2.1), as a function of the wave frequency, it is then possible to identify resonance conditions corresponding to nearly trapped solutions. Then a second approach to the solution is taken consisting of solving the wave equations as an eigenvalues problem, with boundary conditions corresponding to purely outgoing propagation at the right boundary. This formulation of the problem has the advantage of providing a straightforward calculation of the quality factor associated with the cavity, in terms of the mode decay rate and real frequency. The quality factor is proportional to the ratio between the wave period and its decay time.

Following the second approach, the wave equations are then solved fully numerically and the solutions are compared with those obtained from the analytic solution. This comparison is useful in testing the validity of the results obtained with the numerical solution of the wave equations. This is of interest, considering that the same technique is used in the next chapter, in the solution of the more realistic box-model description of mode trapping at the plasmapause.

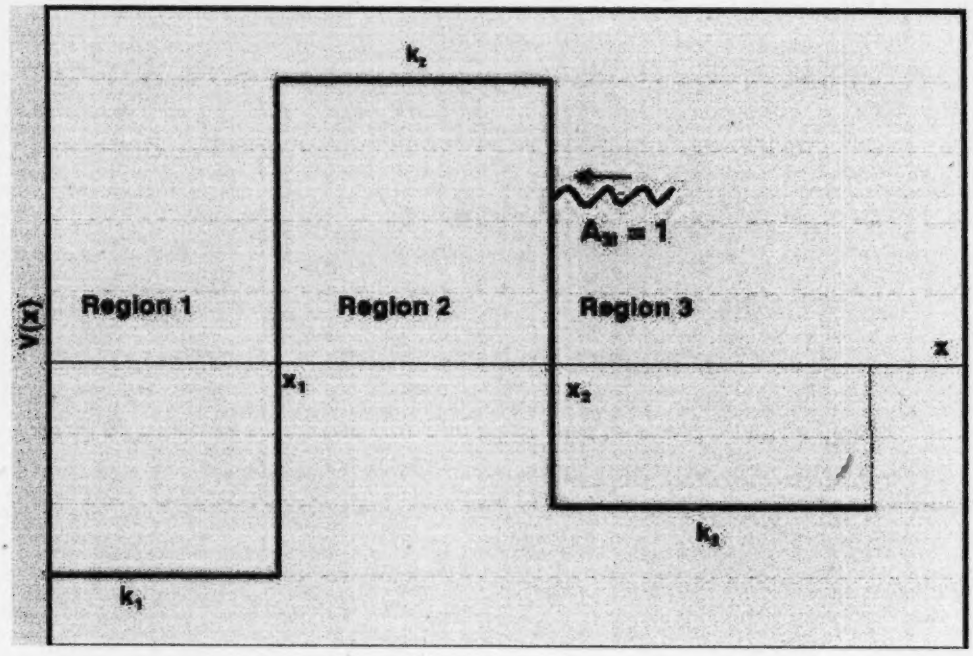

Figure 2.1: Representative of the effective potential.

2.1 Construction of the Wave Function

2.1.1 Continuous spectrum with an incoming wave of unit amplitude

The first solution considered is for the wave amplitude in the well region (region 1 in figure 2.1) as a function of the wave frequency. This is calculated for a wave coming from the right with a unit amplitude. This idealized problem is constructed because it is readily amenable to analytic and numerical solutions. This model problem consists of solving a one dimensional wave equation similar to the Schrödinger equation.

The model wave equation used is;

$$\frac{d^2\psi(x,t)}{dx^2} + \left(\frac{\omega^2}{c^2} - sign(k^2,k)\right)\psi(x,t) = 0, \tag{2.1}$$

where the potential, $V(x)$, is defined as $\frac{\omega^2}{c^2} - sign(k^2,k)$, c is the speed of light, and ω is wave frequency . The function $sign(k^2,k)$ is equal to $|k^2|sign(k)$, and k is the parameter

determining the depth of the potential well (see figure 2.1). The values k_1, k_2, and k_3 in the figure 2.1 represent the k values in regions 1, 2 and 3.

The boundary conditions are taken to be;

1. The incident wave amplitude is equal to 1, or $A_{3I} = 1$ in region 3, where the initial wave is coming from,
2. The wave function is equal to 0 at $x = 0$, $\psi(x,t)|_{x=0} = 0$;

Equation 2.1 will have a solution of the type;

$$\psi(x,t) = Ae^{\mp i\alpha x}, \tag{2.2}$$

where A is the amplitude, and $\alpha = \sqrt{\frac{\omega^2}{c^2} - sign(k^2,k)}$. Looking at the above expression, it can be seen that the solution will be oscillatory when $\frac{\omega^2}{c^2} > sign(k^2,k)$, and that it will be non-oscillatory, decaying or growing when $\frac{\omega^2}{c^2} < sign(k^2,k)$.

Assuming a time dependence of the form $e^{-i\omega t}$, the solution of the wave equation in each region is written as,

1. Region 1, from $x = 0$ to $x = x_1$;
   $\left(A_{1T}e^{-i\alpha_1 x} + A_{1R}e^{i\alpha_1 x}\right)e^{-i\omega t}$,
2. Region 2, from $x = x_1$ to $x = x_2$;
   $\left(A_{2T}e^{-i\alpha_2 x} + A_{2R}e^{i\alpha_2 x}\right)e^{-i\omega t}$,
3. Region 3, for $x > x_2$;
   $\left(A_{3I}e^{-i\alpha_3 x} + A_{3R}e^{i\alpha_3 x}\right)e^{-i\omega t}$.

In these expressions, without the loss of generality, α_1, α_2, and α_3 are assumed to be positive; that is,

$$\alpha_1 = \sqrt{\frac{\omega^2}{c^2} - sign(k_1^2,k_1)},$$
$$\alpha_2 = \sqrt{\frac{\omega^2}{c^2} - sign(k_2^2,k_2)},$$
$$\alpha_3 = \sqrt{\frac{\omega^2}{c^2} - sign(k_3^2,k_3)}.$$

With this convention, it follows that A_{1T}, A_{2T}, $A_{3T}$are amplitudes of waves propagating to the left and A_{1R}, A_{2R}, A_{3R} are the amplitudes of the waves propagating to the right. Then the above boundary conditions 1 and 2 along with the fact that the solution and

its first derivative must be continuous, lead to the following set of algebraic equation:

$$\begin{aligned} A_{1R}(e^{i\alpha_1 x_1} - e^{-i\alpha_1 x_1}) - A_{2R}e^{i\alpha_2 x_1} - A_{2T}e^{-i\alpha 2 x_1} &= 0 \\ \alpha_1 A_{1R}(e^{i\alpha_1 x_1} + e^{-i\alpha_1 x_1}) - \alpha_2 A_{2R}e^{i\alpha_2 x_1} + \alpha_2 A_{2T}e^{-i\alpha 2 x_1} &= 0 \\ A_{2R}e^{i\alpha_2 x_2} + A_{2T}e^{-i\alpha_2 x_2} - A_{3R}e^{i\alpha_3 x_2} &= e^{-i\alpha_3 x_2} \\ \alpha_2 A_{2R}e^{i\alpha_2 x_2} - \alpha_2 A_{2T}e^{-i\alpha_2 x_2} - \alpha_3 A_{3R}e^{i\alpha_3 x_2} &= -\alpha_3 e^{-i\alpha_3 x_2}. \end{aligned}$$

After arranging the set of equations above into a matrix form below equation

$$\begin{pmatrix} (e^{i\alpha_1 x_1} - e^{-i\alpha_1 x_1}) & e^{i\alpha_2 x_1} & e^{-i\alpha_2 x_1} & 0 \\ \alpha_1(e^{i\alpha_1 x_1} + e^{-i\alpha_1 x_1}) & -\alpha_2 e^{i\alpha_2 x_1} & \alpha_2 e^{-i\alpha_2 x_1} & 0 \\ 0 & e^{i\alpha_2 x_2} & e^{-i\alpha_2 x_2} & -e^{i\alpha_3 x_2} \\ 0 & \alpha_2 e^{i\alpha_2 x_2} & -\alpha_2 e^{-i\alpha_2 x_2} & -\alpha_3 e^{i\alpha_3 x_3} \end{pmatrix} \begin{pmatrix} A_{1R} \\ A_{2R} \\ A_{2T} \\ A_{3R} \end{pmatrix}$$
$$= \begin{pmatrix} 0 \\ 0 \\ e^{-i\alpha_3 x_2} \\ -\alpha_3 e^{-i\alpha_3 x_2} \end{pmatrix} \tag{2.3}$$

is obtained. Equation 2.3 is then solved using LU decomposition [33] for a given set of k_1, k_2, k_3, x_1, and x_2 values. Trapped modes are searched by arranging the k values in each region, which in turn determines the characteristics of the potential (see figure 2.1). In the case considered here, x_1 and x_2 are set to 3.141 and 4 respectively, c is set to unity, and the values of k_1, k_2, k_3 are set to -1, 4, and -1. In figure 2.2 the maximum amplitude in region 1 is plotted as a function of the frequency, ω. The peaks are expected to correspond to frequency values associated with quasi-trapped modes. Note that in this analysis, the wave frequency is assumed to be purely real, and it is varied continuously; that is, the waves considered have a continuous spectrum. In the following, the wave frequency will be assumed to be complex, and the resulting spectrum will be discrete.

2.1.2 Discrete spectrum and quality factor - analytic solution

In the study of cavity modes, the quality factor, Q, is a useful parameter to characterize the cavity. The Q factor is proportional to the ratio between the wave period and its decay time: $Q = \pi(\tau/T)$, where τ is the wave decay time and T is its oscillation period. Using $1/T = f = \omega_r/2\pi$, the Q factor is expressed as;

$$Q = \frac{\omega_r \tau}{2},$$

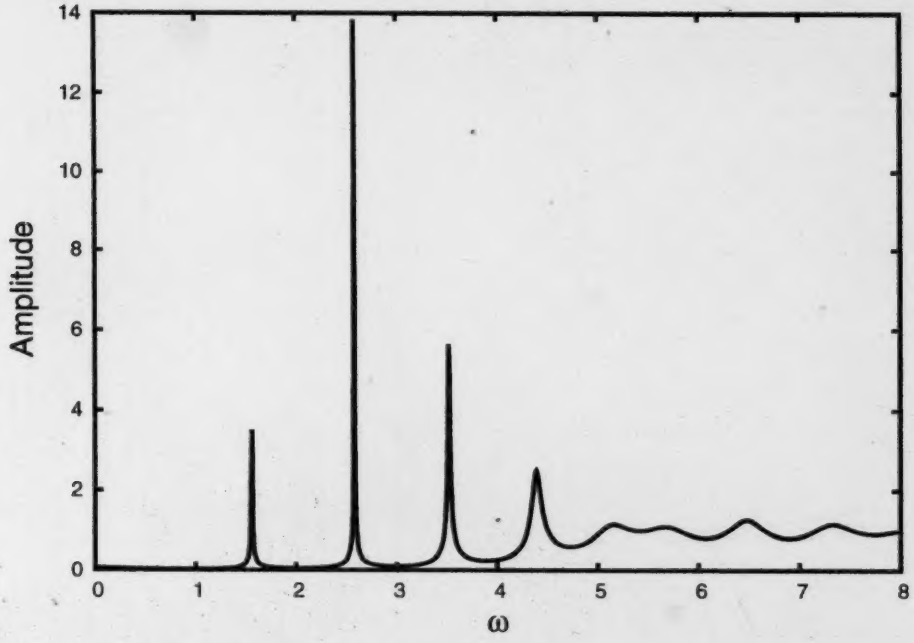

Figure 2.2: Maximum Amplitude A in region 1 as a function of frequency, ω. In this plot the frequency is purely real and continuous. The values of the frequency where the amplitude peaks are seen, are expected to be the resonance frequencies.

and using the relation $\omega_i = 1/\tau$ Q factor equation is obtained as;

$$Q = \frac{\omega_r}{2\omega_i}, \tag{2.4}$$

where, the frequency, ω, is now set to be complex and ω_i is the imaginary part, ω_r is the real part. Equation 2.4 will be used the calculate the Q factor values in the current problem.

Cavity resonances are observed if waves are confined to a finite region of space which is delimited by two classical turning points. This incident can be observed in the assumed potential well if the resonant frequency condition is satisfied. Therefore, in order to find the cavity modes in the potential well the Q factor should be sufficiently high, so that the waves do not decay in a short time, before reaching the potential walls. A high Q factor means that the peak width of the frequency response is narrow and damping

is very small. The decay rate is also associated with the wave tunneling through the barrier.

As stated earlier, the wave equation is solved as a discrete eigenvalue problem. Specifically, the boundary conditions are now assumed to be

1. a vanishing amplitude at the left boundary,

2. a purely outgoing wave propagation at the right boundary

More specifically, in the notation of the previous subsection, the boundary conditions are

$A_{1T} + A_{1R} = 0$

$A_{3I} = 0.$

The spectrum of the eigenvalue problem is calculated numerically using a root finder. Figure 2.5 shows a plot of imaginary part of the frequency as a function of the real part.

The corresponding Q factors can then be calculated, using equation 2.4. The results are shown in figure 2.5 with the stars representing the solutions obtained with the present approach. These results are independent of the length of the system or the position of the right boundary. It is worth emphasizing that in figure 2.5, high values of Q correspond to frequencies of the amplitude peaks in figure 2.2, where the amplitude is plotted as a function of the continuous frequency. Figure 2.3 illustrates the solution for the two lower values of the mode frequency, corresponding to the two highest values of Q. This figure clearly shows the spatial localization of the mode in the well region, and the relatively low amplitude of the leaking (tunneling) wave. For comparison, figure 2.4 shows a wave corresponding to a low Q. From the expression for the Q factor in equation 2.4, it is seen that the high value means low ω_i, which gives longer decay time.

2.1.3 Discrete spectrum and quality factor - numerical solution

In this section the wave equation, equation 2.1, is solved fully numerically using a fourth order Runge-Kutta method. The wave equation has the form

$$y'' + \left(\frac{\omega^2}{c^2} - sign(k^2, k)\right) y = 0. \tag{2.5}$$

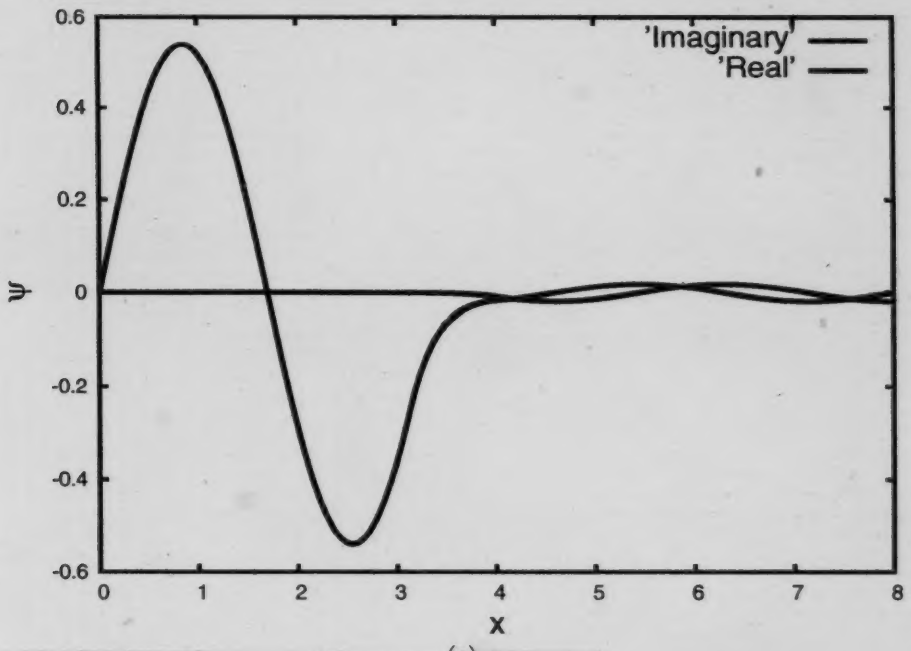

(a)

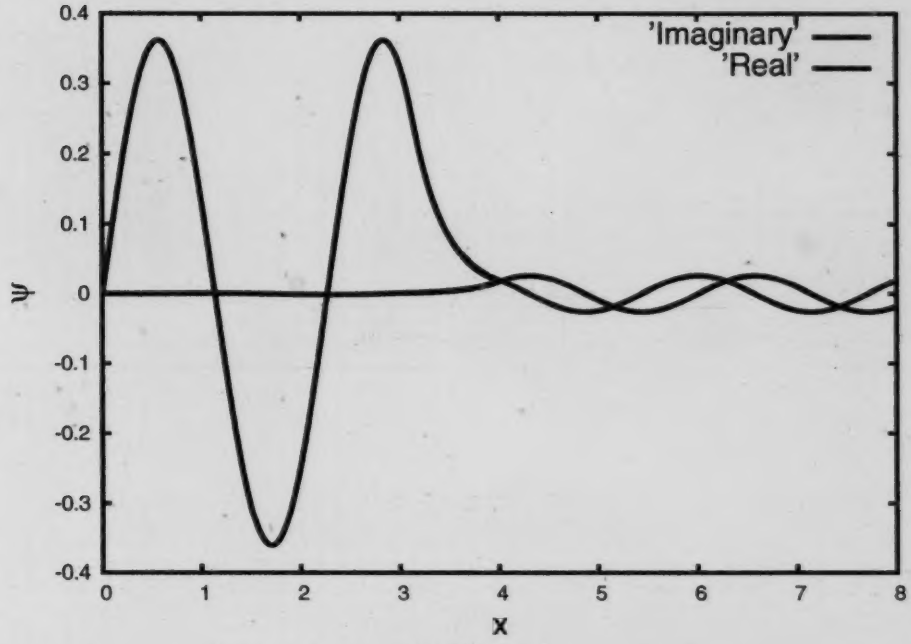

(b)

Figure 2.3: Wave function as a function of distance for two different frequencies that correspond to a high Q factor from the analytical solution. The values used are; $\omega_r = 1.55$, $\omega_i = -4.020 \times 10^{-3}$, $Q = 1937.8$ for figure (a), and $\omega_r = 2.57$, $\omega_i = -1.60 \times 10^{-3}$ and $Q = 801.7$ for figure (b). These correspond to the two largest values of Q in figure 2.5.

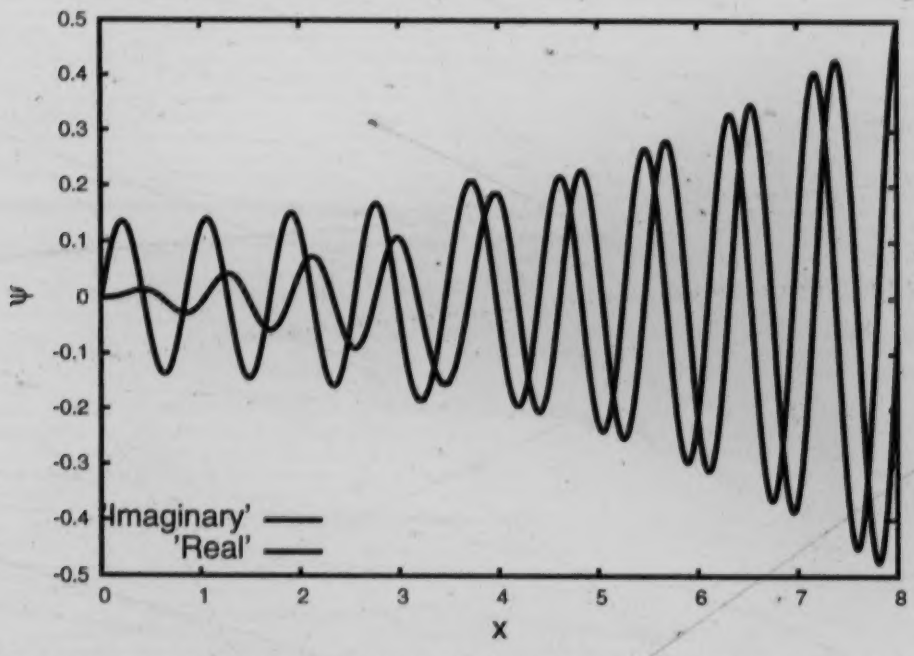

Figure 2.4: Wave function as a function of distance for a frequency that corresponds to a low Q factor. The mode considered corresponds to $\omega_r = 7.31$, $\omega_i = -0.247 \times 10^{-3}$, and $Q = 14.7$. This is a low Q value chosen from figure 2.5.

In order to apply the Runge-Kutta method to the wave equation, the wave function ψ, and its first derivative, ψ', are expressed as,

$$\begin{aligned} \psi &= y_1, \\ \psi' &= y_2, \end{aligned}$$

thus, the equation 2.1 is rewritten as a set of coupled first order ordinary differential equations as,

$$\begin{aligned} \frac{\partial y_1}{\partial x} &= y_2, \\ \frac{\partial y_2}{\partial x} &= -\left(\frac{\omega^2}{c^2} - sign(k^2, k)\right) y_1. \end{aligned}$$

The boundary conditions are the same as in subsection 2.2.2. They correspond to a vanishing amplitude at $x = 0$, and a purely outgoing wave at the right boundary. In order to solve with Runge-Kutta integration, it is now necessary to assume some initial conditions which are specified at $x = 0$. They are
$\psi = 0$ (same as one of the boundary conditions) and,
$\partial\psi/\partial x = y_2 = 1$.
The solution is then integrated up to the right boundary and the eigenfrequencies are determined using a standard root finder, so as to satisfy the right boundary condition

$$\psi(x,t)' - i\alpha_3\psi(x,t) = 0. \tag{2.6}$$

It should be noted that the initial condition, $y_2 = 1$, is of no consequence in this linear eigenvalue problem, as the solution is defined up to an arbitrary multiplicative constant. The wave is assumed to be initiated in region 1 in the figure 2.1, and the eigen-values which satisfy the boundary condition in the region 3 is found. Then the Q factor is calculated using these frequencies, in the same way as with the analytical solutions. The results obtained with this fully numerical approach are in excellent agreement with those presented in subsection 2.2.2 as is apparent from figure 2.5. The number of eigen-frequencies is the same in both approaches, in the entire frequency interval considered. The maximum relative difference in these frequencies is found to be of the of order 10^{-5}. For comparison the frequency and Q factor graphs from both subsections are superposed in figure 2.5. The agreement between the results obtained is this section and those of subsection 2.2.2. is a useful test of the numerical approach to be used in the next chapter. The work done in this chapter, showed that with a symbolic potential of the figure 2.1 it is possible to obtain trapped modes of the compressional waves.

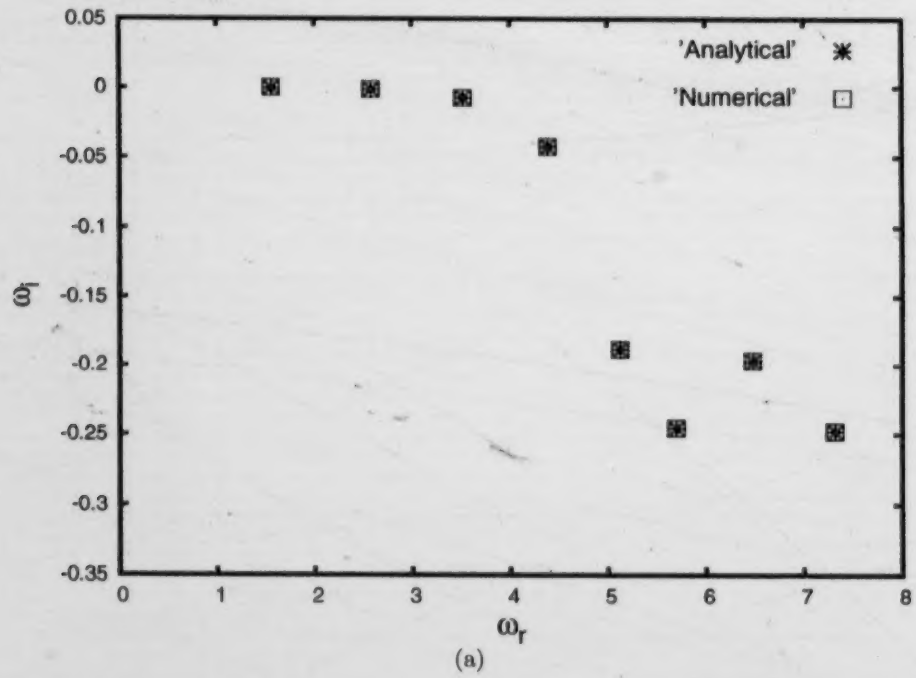

(a)

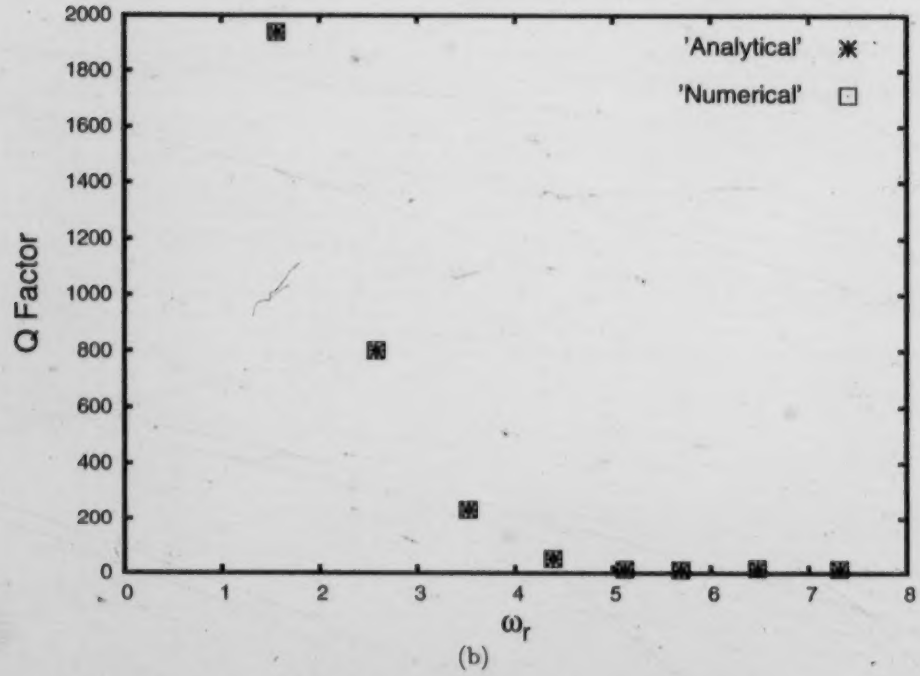

(b)

Figure 2.5: Superposed graphs of frequency spectrums, figure (a), and Q as a function of real frequency(ω_r), figure(b), from analytical and numerical solutions. The good match demonstrates the consistency of the numerical method which will be used in chapter three for a more realistic solution of the problem.

Chapter 3

First Approximation: Box Model

In this chapter the problem of compressional mode trapping in the plasmapause is explored with physically more realistic set of equations. For that purpose, a one dimensional approximate model, the box model, is used. First a governing wave equation is derived in the ideal MHD approximation. This derivation is based on Maxwell's equations, the plasma continuity equation and the equation of momentum conservation. The plasma in the plasmasphere and plasmapause is assumed to be cold, thus pressure effects are neglected. The resulting wave equation is a second order ordinary differential equation. Using a standard technique, this equation can then be transformed into a second order differential equation of the form 2.1, from which an effective potential can readily be identified. The wave equation, combined with the appropriate boundary conditions, then constitutes an eigenvalue problem as in 2.2.3. A numerical solution of this equation then yields discrete mode frequencies from which Q factors can be calculated, as in the previous chapter.

3.1 Construction of the Velocity Wave Function

In this section, an equation is derived for the velocity components of the plasma, in the MHD approximation. The plasma in the plasmasphere and the plasmapause can be approximated as cold. Under these conditions, the thermal pressure, P, is equal to 0.

The set of equations used are;

$$\frac{\partial \rho(\mathbf{r},t)}{\partial t} + \nabla \cdot [\rho(\mathbf{r},t)\mathbf{V}(\mathbf{r},t)] = 0, \tag{3.1}$$

$$\frac{d}{dt}[\rho(\mathbf{r},t)\mathbf{V}(\mathbf{r},t)] = \mathbf{J}(\mathbf{r},t) \times \mathbf{B}(\mathbf{r},t), \tag{3.2}$$

$$\nabla \times \mathbf{E}(\mathbf{r},t) = -\frac{\partial \mathbf{B}(\mathbf{r},t)}{\partial t}, \tag{3.3}$$

$$\nabla \times \mathbf{B}(\mathbf{r},t) = \mu_0 \mathbf{J}(\mathbf{r},t) + \epsilon_0 \mu_0 \frac{\partial \mathbf{E}(\mathbf{r},t)}{\partial t}, \tag{3.4}$$

and ideal MHD condition for the electric field;

$$\mathbf{E}(\mathbf{r},t) = -\mathbf{V}(\mathbf{r},t) \times \mathbf{B}(\mathbf{r},t). \tag{3.5}$$

Where $\mathbf{r} = (x, y, z)$ is the position vector, t is the time, $\mathbf{E}$ is the electric field, $\mathbf{B}$ is the magnetic field, $\mathbf{J}$ is the current density, ρ is the mass density, $\mu_0 = 4\pi \times 10^{-7} N/A^2$ is the permeability of free space, and $\epsilon_0 = 8.85 \times 10^{-12} C^2/Nm^2$ is the permittivity of the free space. Charge neutrality, $n_e = n_i$, is also assumed, thus no electric-field force is present the equation of motion 3.2. In the following, all equations are solved in the linear approximation. Specifically, dependent variables are assumed to be the superposition of an equilibrium value, say g_0, and a perturbed value g_1; $g(\mathbf{r},t) = g_0(\mathbf{r},t) + g_1(\mathbf{r},t)$, where g represents an arbitrary dependent variable. All first order perturbations are assumed to depend on time according to $g(\mathbf{r},t) = g(\mathbf{r})e^{-i\omega t)}$, where ω is the mode frequency.

Linearization:

Equations 3.1, 3.2, 3.3, 3.4, and 3.5 are then linearized using the following ansatz;

$$\begin{aligned} \mathbf{E} &= \mathbf{E}_0 + \mathbf{E}_1 \\ \mathbf{V} &= \mathbf{V}_0 + \mathbf{V}_1 \\ \mathbf{B} &= \mathbf{B}_0 + \mathbf{B}_1 \\ \rho &= \rho_0 + \rho_1 \\ \mathbf{J} &= \mathbf{J}_0 + \mathbf{J}_1 \end{aligned} \tag{3.6}$$

From this point on, for simplicity, ρ and $\mathbf{V}$ are used instead of $\rho(\mathbf{r},t)$ and $\mathbf{V}(\mathbf{r},t)$ respectively and the same is used with the other variables, $\mathbf{E}$, $\mathbf{B}$, and $\mathbf{J}$.

Starting with equation 3.1, the continuity equation, first the values of mass density,

ρ, and velocity, $\mathbf{V}$, are replaced from the set of equation 3.6 to yield

$$\begin{aligned} \frac{\partial}{\partial t}(\rho_0+\rho_1)+\nabla\cdot[(\rho_0+\rho_1)(\mathbf{V}_0+\mathbf{V}_1)] &= 0, \\ \frac{\partial\rho_0}{\partial t}+\frac{\partial\rho_1}{\partial t}+\nabla\cdot[\rho_0\mathbf{V}_0+\rho_0\mathbf{V}_1+\rho_1\mathbf{V}_0+\rho_1\mathbf{V}_1] &= 0. \end{aligned}$$

Using the facts that ρ_0 is constant in time, $\partial\rho_0/\partial t = 0$, $V_0 = 0$, and neglecting second order term, the above equation becomes;

$$\frac{\partial\rho_1}{\partial t}+\nabla\cdot(\rho_0\mathbf{V}_1)=0. \tag{3.7}$$

Then the equation of motion, 3.2, is linearized following the same approach as above;

$$\begin{aligned} \frac{d}{dt}[(\rho_0+\rho_1)(\mathbf{V}_0+\mathbf{V}_1)] &= (\mathbf{J}_0+\mathbf{J}_1)\times(\mathbf{B}_0+\mathbf{B}_1), \\ \frac{d}{dt}[\rho_0\mathbf{V}_0+\rho_0\mathbf{V}_1+\rho_1\mathbf{V}_0+\rho_1\mathbf{V}_1] &= \mathbf{J}_0\times\mathbf{B}_0+\mathbf{J}_0\times\mathbf{B}_1+\mathbf{J}_1\times\mathbf{B}_0+\mathbf{J}_1\times\mathbf{B}_1. \end{aligned}$$

The the zeroth and the second order terms are neglected. The values $V_0 = 0$, and B_0 and ρ_0 are constant in time, $\partial\mathbf{B}_0/\partial t = 0$ and $\partial\rho_0/\partial t = 0$, are used. In order to approximate an actual dipole geometry, the value $\nabla\times\mathbf{B}_0$ is assumed to vanish, thus $J_0 = 0$ which results in

$$\rho_0\frac{d\mathbf{V}_1}{dt}=\mathbf{J}_1\times\mathbf{B}_0.$$

Then with the reminder that, $d(\mathbf{V}_1)/dt$ is the convective derivative, that is;

$$\frac{d}{dt}(\mathbf{V}_1)=\frac{\partial\mathbf{V}_1}{\partial t}+(\nabla\cdot\mathbf{V}_1)\mathbf{V}_1,$$

and neglecting the non-linear term, $(\nabla\cdot\mathbf{V}_1)\mathbf{V}_1$, the final version of the linearized equation of motion is obtained as,

$$\rho_0\frac{\partial\mathbf{V}_1}{\partial t}=\mathbf{J}_1\times\mathbf{B}_0. \tag{3.8}$$

Finally, following the same steps, the linearized forms of Ampere's law, Faraday's law, and the ideal MHD law, the equations 3.3, 3.4, and 3.5 respectively, are obtained as;

$$\nabla\times\mathbf{E}_1 = -\frac{\partial\mathbf{B}_1}{\partial t}, \tag{3.9}$$

$$\nabla\times\mathbf{B}_1 = \mu_0\mathbf{J}_1+\epsilon_0\mu_0\frac{\partial\mathbf{E}_1}{\partial t}, \tag{3.10}$$

and,

$$\mathbf{E}_1 = -\mathbf{V}_1 \times \mathbf{B}_0. \tag{3.11}$$

After the linearization, the value of $\mathbf{J}_1$ is obtained from the equation 3.10 as;

$$\mathbf{J}_1 = \frac{1}{\mu_0}\left(\nabla \times \mathbf{B}_1 - \epsilon_0\mu_0\frac{\partial \mathbf{E}_1}{\partial t}\right),$$

and replaced in the equation 3.8, the linearized equation of motion, which becomes

$$\rho_0\frac{\partial \mathbf{V}_1}{\partial t} = \frac{1}{\mu_0}\left(\nabla \times \mathbf{B}_1 - \epsilon_0\mu_0\frac{\partial \mathbf{E}_1}{\partial t}\right) \times \mathbf{B}_0.$$

With the replacement of $\mathbf{E}_1$ from the linearized form of equation 3.11

$$\rho_0\frac{\partial \mathbf{V}_1}{\partial t} = \frac{1}{\mu_0}\left(\nabla \times \mathbf{B}_1 + \epsilon_0\mu_0\frac{\partial(\mathbf{V}_1 \times \mathbf{B}_0)}{\partial t}\right) \times \mathbf{B}_0 \tag{3.12}$$

is obtained. Then using the equations 3.9 and 3.11 the value $\mathbf{B}_1$ is obtained as;

$$-\frac{\partial \mathbf{B}_1}{\partial t} = \nabla \times \mathbf{E}_1 = -\nabla \times (\mathbf{V}_1 \times \mathbf{B}_0).$$

Using the assumption;

$$g(x, y, z, t) \approx e^{-i\omega t}, \tag{3.13}$$

the value $\partial/\partial t$ is replaced by $-i\omega$. After this replacement the perturbation field, $\mathbf{B}_1$, is found as;

$$\begin{aligned} -i\omega\mathbf{B}_1 &= \nabla \times (\mathbf{V}_1 \times \mathbf{B}_0) \\ \mathbf{B}_1 &= -\frac{1}{i\omega}[\nabla \times (\mathbf{V}_1 \times \mathbf{B}_0)] \end{aligned} \tag{3.14}$$

Equation 3.14 is substituted in the equation 3.12 and the result is;

$$-i\omega\rho_0\mathbf{V}_1 = \frac{1}{\mu_0}\left[\nabla \times \left(-\frac{1}{i\omega}[\nabla \times (\mathbf{V}_1 \times \mathbf{B}_0)]\right) + \epsilon_0\mu_0\frac{\partial(\mathbf{V}_1 \times \mathbf{B}_0)}{\partial t}\right] \times \mathbf{B}_0, \tag{3.15}$$

The equation 3.15 is arranged as;

$$-i\omega\rho_0\partial\mathbf{V}_1 = -\frac{1}{\mu_0 i\omega}\left(\nabla \times [\nabla \times (\mathbf{V}_1 \times \mathbf{B}_0)] \times \mathbf{B}_0\right) + \epsilon_0\left(\frac{\partial(\mathbf{V}_1 \times \mathbf{B}_0)}{\partial t}\right) \times \mathbf{B}_0,$$

Dividing each side by ρ_0 and using the fact that $\mathbf{B}_0$ is constant in time

$$\frac{\partial \mathbf{V}_1}{\partial t} = -\frac{1}{\mu_0 \rho_0 i\omega} (\nabla \times [\nabla \times (\mathbf{V}_1 \times \mathbf{B}_0)] \times \mathbf{B}_0) + \frac{\epsilon_0}{\rho_0} (-i\omega \mathbf{V}_1 \times \mathbf{B}_0) \times \mathbf{B}_0 \qquad (3.16)$$

is obtained. Equation 3.16 is then rewritten using the vector relation,

$$\nabla \times (\mathbf{A} \times \mathbf{B}) = \mathbf{A}(\nabla \cdot \mathbf{B}) - \mathbf{B}(\nabla \cdot \mathbf{A}) + (\mathbf{B} \cdot \nabla)\mathbf{A} - (\mathbf{A} \cdot \nabla)\mathbf{B}.$$

Equation 3.16 for the perturbed velocity can then be written component by component to yield a system of three coupled partial differential equations in three dimensions. When combined with the appropriate boundary conditions, this then constitutes a three dimensional eigenvalue problem which could be solved numerically. For simplicity, however, we now adopt a common approximation used in the context of magnetospheric wave dynamics: the box model (see figures 3.1 and 3.2). In this approximation, mag-

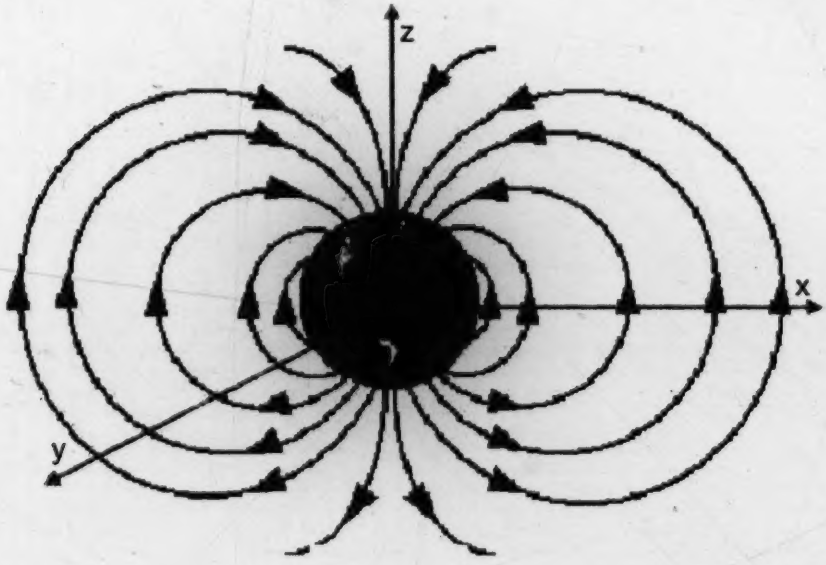

Figure 3.1: Illustration of the coordinate system for the box model of the magnetosphere. The Cartesian coordinates, x, y, and z are representing the dipole coordinates, L, λ, ϕ respectively. The magnetic field lines are approximated to be constant along z, the north-south direction.

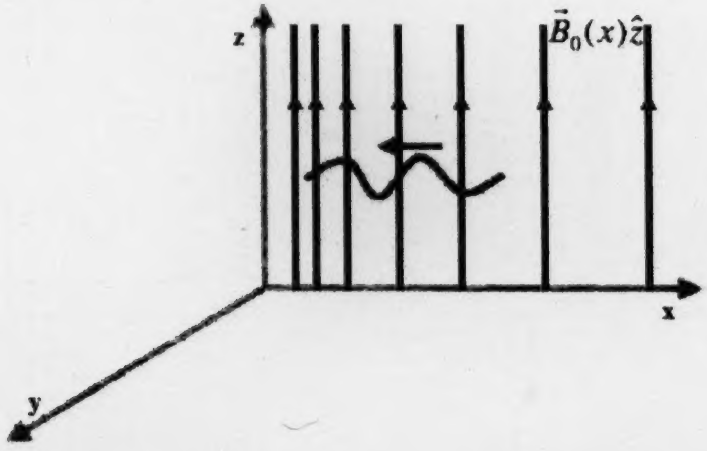

Figure 3.2: Cartesian coordinates, x, y, and z are shown above with the straightened magnetic field lines of the box model. The wave drawn represents the compressional wave traveling across the magnetic field lines.

netic field lines are treated as if they were straight, and all of the same length and only the variation of the magnetic field intensity in the direction perpendicular to the $\mathbf{B}$ is taken into account. The problem can then be formulated in rectangular geometry, with $\mathbf{B}$ oriented along the z coordinate and the magnitude of B varying in the x coordinate as in figure 3.2, where x, y , z coordinates correspond to radial , azimuthal and north-south coordinates respectively as in figure 3.1. None fo the equilibrium physical quantities are assumed to vary in the y and z directions; that is, these coordinates are ignorable. As a result, the dependence of perturbed quantities in these variables may be assumed to be of the form

$$g_1(x, y, z) \approx g_1(x)e^{i(k_y y + k_z z)}.$$

Equation 3.16 is rewritten by replacing the operator ∇ by;

$$\nabla = \left(\frac{\partial}{\partial x}, ik_y, ik_z\right)$$

for the velocity. As for the values $\mathbf{B}_0$ and ρ_0 the x dependence in the magnetosphere will be used and as mentioned before they are assumed to be constant in y, z, and t. Making

use of these assumptions, equations for V_{1x}, V_{1y} , and V_{1z} are written separately as;
X component;

$$\frac{V_A^2}{\omega^2}\frac{\partial^2 V_{1x}}{\partial x^2}+\left(2\frac{V_A^2}{\omega^2}\frac{1}{B_0(x)}\frac{\partial B_0(x)}{\partial x}\right)\frac{\partial V_{1x}}{\partial x} + \left(1-\frac{V_A^2k_z^2}{\omega^2}+\frac{V_A^2}{c^2}+\frac{V_A^2}{\omega^2}\frac{1}{B_0(x)}\frac{\partial^2 B_0(x)}{\partial x^2}\right)V_{1x}$$

$$+ik_y\frac{V_A^2}{\omega^2}\frac{\partial V_{1y}}{\partial x}+ik_y\frac{V_A^2}{\omega^2}\frac{1}{B_0(x)}\frac{\partial B_0(x)}{\partial x}V_{1y} = 0 \qquad (3.17)$$

Y component;

$$ik_y\frac{V_A^2}{\omega^2}\frac{\partial V_{1x}}{\partial x}+ik_y\left(\frac{V_A^2}{\omega^2}\frac{1}{B_0(x)}\frac{\partial B_0(x)}{\partial x}\right)V_{1x}+\left(1-\frac{V_A^2}{\omega^2}(k_y^2+k_z^2)+\frac{V_A^2}{c^2}\right)V_{1y}=0 \quad (3.18)$$

Z component;
$V_{1z}=0$
where, $B_0(x)$ is the background magnetic field on the equatorial plane, $B_0(x)=B_E/L^3$, $B_E=3.11\times10^{-5}T$ is the equatorial magnetic field on the surface of the Earth, L is the equatorial distance from the centre of the Earth in terms of Earth radii(R_E), and V_A is the Alfvén speed, $V_A=B_0(x)/\sqrt{\rho_0\mu_0}$. The z component is found to be equal to zero as expected in the cold plasma approximation.

With a change of variables;
$v_x=V_{1x}$,
$v_y=iV_{1y}$,
$v_z=iV_{1z}$,
equation 3.17 then turns into;

$$\frac{V_A^2}{\omega^2}\frac{\partial^2 v_x}{\partial x^2}+\left(2\frac{V_A^2}{\omega^2}\frac{1}{B_0(x)}\frac{\partial B_0(x)}{\partial x}\right)\frac{\partial v_x}{\partial x} + \left(1-\frac{V_A^2k_z^2}{\omega^2}+\frac{V_A^2}{c^2}+\frac{V_A^2}{\omega^2}\frac{1}{B_0(x)}\frac{\partial^2 B_0(x)}{\partial x^2}\right)v_x$$

$$+k_y\frac{V_A^2}{\omega^2}\frac{\partial v_y}{\partial x}+k_y\frac{V_A^2}{\omega^2}\frac{1}{B_0(x)}\frac{\partial B_0(x)}{\partial x}v_y = 0, \qquad (3.19)$$

and equation 3.18 is first multiplied by $-i$ and then the change of variable is applied which gives the result as;

$$k_y\frac{V_A^2}{\omega^2}\frac{\partial v_x}{\partial x}+k_y\left(\frac{V_A^2}{\omega^2}\frac{1}{B_0(x)}\frac{\partial B_0(x)}{\partial x}\right)v_x-\left(1-\frac{V_A^2}{\omega^2}(k_y^2+k_z^2)+\frac{V_A^2}{c^2}\right)v_y=0 \qquad (3.20)$$

Equations 3.19 and 3.20 are then written symbolically as;

$$A_1 v_x'' + A_2 v_x' + A_3 v_x + A_4 v_y' + A_5 v_y = 0 \quad (3.21)$$

$$B_1 v_x' + B_2 v_x + B_3 v_y = 0 \quad (3.22)$$

Where $A_1, A_2, A_3, A_4, A_5, B_1, B_2$, and B_3 are as follows:

$$\begin{aligned}
A_1 &= \frac{V_A^2}{\omega^2}, \\
A_2 &= \frac{1}{\omega^2}\left(2V_A^2 \frac{1}{B_0(x)} \frac{\partial B_0(x)}{\partial x}\right), \\
A_3 &= 1 - \frac{V_A^2 k_z^2}{\omega^2} + \frac{V_A^2}{c^2} + \frac{V_A^2}{\omega^2} \frac{1}{B_0(x)} \frac{\partial^2 B_0(x)}{\partial x^2}, \\
A_4 &= k_y \frac{V_A^2}{\omega^2}, \\
A_5 &= k_y \left(\frac{V_A^2}{\omega^2} \frac{1}{B_0(x)} \frac{\partial B_0(x)}{\partial x}\right), \\
B_1 &= ky \frac{V_A^2}{\omega^2}, \\
B_2 &= k_y \left(\frac{V_A^2}{\omega^2} \frac{1}{B_0(x)} \frac{\partial B_0(x)}{\partial x}\right), \\
B_3 &= \frac{V_A^2}{\omega^2}(k_y^2 + k_z^2) - \frac{V_A^2}{c^2} - 1.
\end{aligned}$$

As a last step, the velocity wave function, the y component of the velocity, v_y, and its first derivative, v_y', are written in terms of v_x, v_x', and v_x'', using equation 3.22 and substituted in the equation 3.21. The final equation for the x component of the velocity, v_x, becomes;

$$D_1 v_x'' + D_2 v_x' + D_3 v_x = 0 \quad (3.23)$$

where,

$$\begin{aligned}
D_1 &= A_1 + A_4 \chi_1, \\
D_2 &= A_2 + A_4(\chi_1' + \chi_2) + A_5 \chi_1, \\
D_3 &= A_3 + A_4 \chi_2' + A_5 \chi_2, \\
\chi_1 &= -\frac{B_1}{B_3}, \\
\chi_2 &= -\frac{B_2}{B_3}.
\end{aligned}$$

I am interested in the component v_x since it corresponds to the compressional mode. Equation 3.23 is than solved numerically which is explained explicitly in section 3.3. In order to solve for v_x, a fit is made for the plasmasphere density profile as explained in section 3.2.

3.1.1 Calculation of the energy density

A calculation of the total energy density is needed so as to better parameterize the trapped compressional modes. When the total energy density is plotted as a function of distance from the Earth, L, a localization in the region of plasmapause would show clearly the existence of trapped or quasi-trapped modes. If there exist trapped modes in the region, the total energy would accumulate as a result of repeated reflections of the mode.

The energy density is calculated using the equations;

$$U_{emg} = \frac{1}{2}\epsilon_0 E^2 + \frac{B^2}{2\mu_0} \tag{3.24}$$

for the electromagnetic energy, and;

$$U_{kin} = \frac{1}{2}\rho v^2, \tag{3.25}$$

for the kinetic energy density. The total energy density would be,

$$\begin{aligned} U_{tot} &= U_{emg} + U_{kin} \\ &= \frac{1}{2}\epsilon_0 E^2 + \frac{B^2}{2\mu_0} + \frac{1}{2}\rho v^2. \end{aligned}$$

With the help of equations 3.6 the total energy density, is linearized as;

$$U_{tot} = \frac{1}{2}\left(\epsilon_0 E_1^2 + \frac{1}{\mu_0}[B_0^2 + B_1^2] + \rho_0 V_1^2\right).$$

Only the perturbed energy density, which is the part associated with the wave, is considered, and thus the term associated with B_0 is not included, and the above equation becomes

$$U_{tot} = \frac{1}{2}\left(\epsilon_0 E_1^2 + \frac{1}{\mu_0} B_1^2 + \rho_0 V_1^2\right). \tag{3.26}$$

Then E_1 is replaced by $-\mathbf{V}_1 \times \mathbf{B}_0$ from equation 3.11, and the real part of the E and B values are used for energy density calculation. The real part of the electric field is found

to be

$$\begin{aligned} E_{1x(real)} &= -B_0(x)V_{1y}\cos(\omega t), \\ E_{1y(real)} &= B_0(x)V_{1x}\cos(\omega t), \\ E_{1z(real)} &= 0, \end{aligned}$$

and the value needed for the total energy density calculation, E^2, is calculated as;

$$E^2_{1(real)} = \cos^2(\omega t)B_0^2(x)(V_{1x}^2 + V_{1y}^2).$$

B_1 is found using equation 3.9 and the real part of it is calculated as,

$$\begin{aligned} B_{1x(real)} &= -\frac{k_z}{\omega}[B_0(x)V_{1x}\cos(\omega t)], \\ B_{1y(real)} &= -\frac{k_z}{\omega}[B_0(x)V_{1y}\cos(\omega t)], \\ B_{1z(real)} &= -\frac{1}{\omega}\frac{\partial}{\partial x}[B_0(x)V_{1x}]\sin(\omega t) + \frac{ky}{\omega}[B_0(x)V_{1y}\cos(\omega t)], \end{aligned}$$

and the values $B^2_{1(real)}$ is calculated as

$$\begin{aligned} B^2_{1(real)} &= \frac{k_z^2}{\omega^2}[B_0(x)^2 cos^2(\omega t)(V_{1x}^2 + V_{1y}^2)] + \frac{1}{\omega^2}\left\{\frac{\partial}{\partial x}[B_0(x)V_{1x}]\right)^2 \sin^2(\omega t) \\ &- \frac{2}{\omega^2}\left(\frac{\partial}{\partial x}[B_0(x)V_{1x}]k_y B_0(x)V_{1y}\cos(\omega t)\sin(\omega t)\right) + \frac{k_y^2}{\omega^2}B_0(x)^2 V_{1y}^2 cos^2(\omega t). \end{aligned}$$

The values $E^2_{1(real)}$ and $B^2_{1(real)}$ are substituted in the equation 3.26. The total energy density is then

$$\begin{aligned} U_{tot} &= \frac{1}{2}[\epsilon_0 B_0(x)^2\cos^2(\omega t)(v_x^2 + v_y^2)] + \frac{1}{2\mu_0\omega^2}[k_z^2 B_0(x)^2\cos^2(\omega t)(v_x^2 + v_y^2)] \\ &+ \frac{1}{2\mu_0\omega^2}\left(\left[\frac{\partial}{\partial x}B_0(x)v_x\right]^2 \sin^2(\omega t) - 2\frac{\partial}{\partial x}[B_0(x)v_x]k_y v_y B_0(x)\cos(\omega t)\sin(\omega t)\right) \\ &+ \frac{1}{2\mu_0\omega^2}[k_y^2 B_0(x)^2 v_y^2\cos^2(\omega t)] + \frac{1}{2}[\rho_0(x)(v_x^2 + v_y^2 + v_z^2)]. \end{aligned}$$

In the equation above the velocity components, V_{1x}, V_{1y}, and $V_{1z}$are replaced by, v_x, v_y, and v_z respectively, and V_1^2 is replaced by, $v_x^2 + v_y^2 + v_z^2$. Also as with the components of the electric and magnetic fields, only the real parts of the velocity values are used.

As a result the time-averaged energy density is obtained as

$$\begin{aligned}\langle U_{tot}\rangle &= \frac{1}{8}[\epsilon_0 B_0(x)^2(v_x^2+v_y^2)] + \frac{1}{8\mu_0\omega^2}\left[k_z^2 B_0(x)^2(v_x^2+v_y^2) + k_y^2 B_0(x)^2 v_y^2\right] \quad (3.27)\\ &+ \frac{1}{8\mu_0\omega^2}\left(\left[\frac{\partial B_0(x)}{\partial x}\right]^2 v_x^2 + \left[\frac{\partial v_x}{\partial x}\right]^2 B_0(x)^2\right) + \frac{1}{4}[\rho_0(x)(v_x^2+v_y^2+v_z^2)].\end{aligned}$$

The sign $\langle\rangle$ is used to denote the time average over a complete cycle. The average of $\cos^2(\omega t)$ and $\sin^2(\omega t)$ over a complete cycle is $1/2$, and average of $\cos(\omega t)$ and $\sin(\omega t)$ over a complete cycle are 0.

3.1.2 Calculation of the effective potential

The wave equation, equation 3.23, derived above is a second order differential equation with a non zero term multiplying the first derivative. Using a change of dependent variable, it is possible to reduce this equation to one where the first derivative term is absent. By analogy with equation 2.1 it is then possible to identify an effective potential. The change of dependent variable is obtained by first representing the perturbed velocity v_x as a product of two unknown functions,

$$v_x = gh. \quad (3.28)$$

Then the first and the second derivatives of v_x are found as

$$v_x' = g'h + h'g, \quad (3.29)$$

$$v_x'' = h''g + g''h + 2g'h'. \quad (3.30)$$

After substituting equations 3.28, 3.29, and 3.30 in 3.23, one finds

$$D_1 g h'' + (2D_1 g' + D_2 g)h' + (D_1 g'' + D_2 g' + D_3 g)h = 0.$$

In order to obtain an equation of the form 2.1, g is assumed to satisfy

$$2D_1 g' + D_2 g = 0. \quad (3.31)$$

The wave equation is then of the form

$$h'' - V_{pot} h = 0$$

where V_{pot} is the effective potential function, expressed as

$$V_{pot} = -\frac{1}{D_1 g}(D_1 g'' + D_2 g' + D_3 g)h. \tag{3.32}$$

The function g in 3.32 is obtained from solving the equation 3.31 above. The result is

$$g = e^{\int_{x_0}^{x} -\frac{D_2}{2D_1}\, dx'}$$

where x_0 is an arbitrary position.

3.2 Fitting a Function to a Plasmasphere Density Profile

The representation of the aforementioned abrupt drop of the density, ρ_0, is conveniently obtained with an analytical fit of the density profile in the plasmapause. The function used is

$$\rho_0(x) = \rho_{in} W(x) + \rho_{out}[1 - W(x)], \tag{3.33}$$

where, $\rho_{in} = M_{in}e^{-x/50}$, $\rho_{out} = M_{out}e^{-x/5}$, and M_{in}, M_{out} represent the mass density inside and just outside the plasmasphere respectively. The function W(x),

$$W(x) = \frac{1}{2}\left[1 - tanh\left(\frac{x - R_0}{\delta}\right)\right], \tag{3.34}$$

is the weight function providing the sharp decline at the plasmapause. The value x is the distance from the Earth, R_0 is the plasmapause position and δ is an adjustable transition length;that is, the length over which the sudden density drop is observed. Distances are expressed in terms of R_E, i.e L value. The values M_{in} and M_{out} are expressed as

$$M_{in} = N_{in} m_p e^{x_{in}/50}, \tag{3.35}$$

$$M_{in} = N_{out} m_p e^{x_{out}/5} \tag{3.36}$$

where N_{in} and N_{out} are the number densities x_{in} and x_{out} are the scale lengths for inside and outside of the plasmasphere respectively, and m_P is the proton mass. These are adjustable parameters, together with R_0 and δ, are used to fit a certain density profile in the numerical program described in section 3.3. As an illustration of the use of the density function, 3.33, a set of value is taken from curve 2 in figure 1.11, and fitted with the expression in equation 3.33. The resulting mass density is plotted as a function of L in figure 3.3 which is a good approximation (See figure 1.11 profile 2 for comparison).

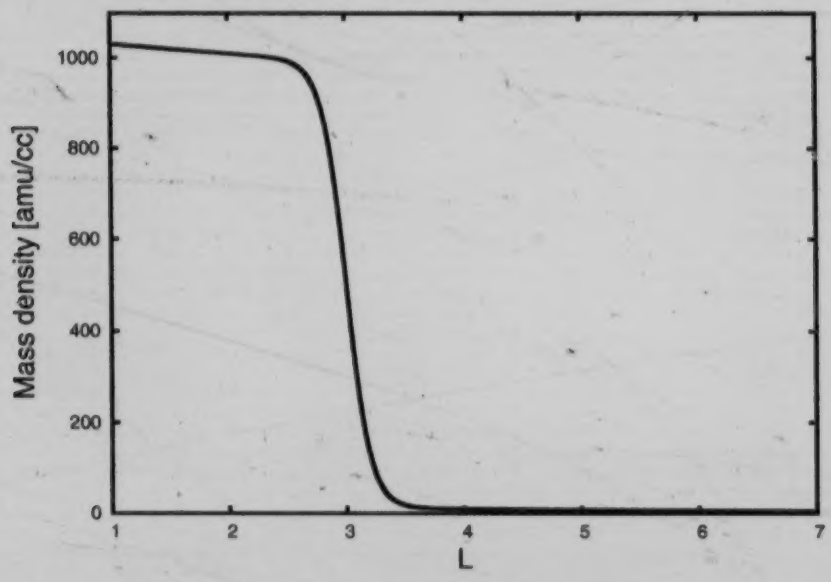

Figure 3.3: Illustration of function 3.33 is used to fit the density profile of the plasmasphere. The values in equations 3.35 and 3.36 are set to , $N_{in} = 1000$, $N_{out} = 10$, $x_{in} = 2.5$, $x_{out} = 3.8$, $R_0 = 3$, and $\delta = 0.2$, corresponding approximately to profile 2 in figure 1.11.

3.2.1 The Alfvén velocity profile

With the density profile illustrated in figure 3.3, the Alfvén velocity is plotted as a function of L to investigate the profile that would possibly support trapped modes. Therefore in the Alfvén velocity equation,

$$V_A(x) = \frac{B_0(x)}{\sqrt{\mu_0 \rho_0(x)}},$$

the equation 3.33 is used for ρ_0, and $B_0(x) = B_E/L^3$. The resulting plot, shown in figure 3.4, is a profile that supports quasi-trapped modes as illustrated in figure 1.12 c and d. The strong similarity with the potential profiles in figures 1.12 c and d of chapter 1 section 1.4.5 is obvious in figure 3.4. Thus, depending on the frequency of the waves, quasi trapped modes of the compressional wave is expected (see explanation in section 1.4.5). This work is done numerically in the following section.

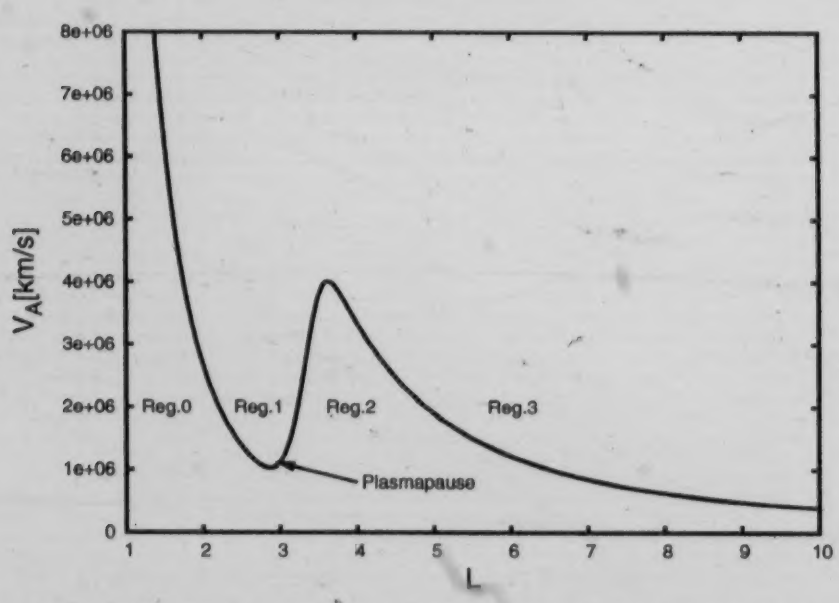

Figure 3.4: Alfvén velocity as a function of L values for the density profile of the figure 3.33. The profile is similar to that of the potential well in figure 1.12 c and d section 1.4.5. Thus the quasi trapped modes are possible in the plasmapause depending on the frequency of the waves.

3.3 Numerical Solution

In this section the final equation, 3.23, for the compressional wave, is solved numerically using a Runge-Kutta integration. Boundary conditions corresponding to outgoing waves are imposed, as in section 2.2.2, using the WKB approximation for the solution at the right boundary. Equation 3.23,

$$D_1 v_x'' + D_2 v_x' + D3vx = 0,$$

is formally rewritten as,

$$D_1 v_x'' + \frac{1}{\epsilon} D_2 v_x' + \frac{1}{\epsilon^2} D_3 v_x = 0 \tag{3.37}$$

where ϵ represent a small parameter. Then a solution of a type

$$v_x = exp\left(\epsilon^{-1} g_0(x) + \epsilon^0 g_1(x) + \epsilon^1 g_2(x) + \ldots\right) \tag{3.38}$$

is assumed and v_x', v_x'' are calculated. Subsituting v_x, v_x' and v_x'' in 3.37 and including the terms up to first order then yields

$$D_1\left[\left(\frac{1}{\epsilon}g_0(x)'' + g_1(x)''\right) + \left(\frac{1}{\epsilon}g_0(x)' + g_1(x)'\right)^2\right]v_x + \frac{1}{\epsilon}D_2\left(\frac{1}{\epsilon}g_0(x)' + g_1(x)'\right)v_x + \frac{1}{\epsilon^2}D_3 v_x = 0.$$

Rewriting this equation order by order, starting with the dominant terms in the asymptotic expansion then yields

$$\frac{1}{\epsilon^2}\left(D_1[g_0(x)']^2 + D_2 g_0(x)' + D_3\right) = 0, \tag{3.39}$$

$$\frac{1}{\epsilon}\left(D_1 g_0(x)'' + 2D_1 g_0(x)' g_1(x)' + D_2 g_1(x)'\right) = 0. \tag{3.40}$$

Equation 3.40 is solved for the function $g_1(x)'$ in terms of $g_0(x)''$ and $g_0(x)'$ as

$$g_1(x)' = -\frac{g_0(x)''}{\frac{D_2}{D_1} + 2g_0(x)'} \tag{3.41}$$

Equation 3.39 is solved for $g_0(x)'$ using quadratic formula,

$$g_0(x)' = \frac{-D_2 \pm \sqrt{\Delta}}{2D_1}$$

where

$$\Delta = D_2^2 - 4D_1 D_3.$$

The second derivative, $g_0(x)''$, is calculated numerically using central differences and these values are used to determine the values $g_1(x)'$ in equation 3.41.

In setting the boundary value, the wave is assumed to be initiated in region 1, corresponding to the plasmapause in figure 3.4 and the boundary value is set in region 3, corresponding to an outgoing wave with the help of equation 3.38. From the derivative of v_x in equation 3.38,

$$v_x' = \left(\frac{1}{\epsilon}g_0(x)' + g_1(x)'\right)v_x,$$

the boundary condition is set as

$$v_x' - \left(\frac{1}{\epsilon}g_0(x)' + g_1(x)'\right)v_x\Big|_{L=L_{max}} = 0. \tag{3.42}$$

In order to prevent the singularities the mathematical expressions in equation 3.23, as in section 1.2.3, the frequency is considered to be complex, $\omega = \omega_r + i\omega_i$. The numerical program used to find the results first calculates the functions D_1, D_2, D_3, $\rho_0(x)$, $B_0(x)$, and $V_A(x)$. Then $g_0(x)'$, $g_1(x)'$ are calculated using D_1, D_2, and D_3. Equation 3.23 is solved using a fourth order Runge-Kutta method, and the complex frequencies that satisfy the boundary condition, are calculated using a root finder. Since the frequency is complex, all values that depend on it are also complex. Finally, the roots of the boundary value problem, equation 3.42, are used to calculate the Q factor from $Q = \omega_r/2\omega_i$.

The same analysis is applied to three different density profiles obtained from IMAGE and SAMNET magnetometer arrays during geomagnetic storms of September 1998, May 2001, and October 2003 [9]. This is explained briefly in following sections.

3.4 Case Studies

In this section three different profiles of the plasmapause are examined for the possibility of trapped compressional waves. The results of the numerical solutions of section 3.3 is presented for each profile for different sets of parameters. The parameters in this problem are the k_y and k_z wave numbers. In the box model, waves produce standing patterns with wave numbers quantized as
$k_y = \frac{m}{R_0}$ and
$k_z = \frac{n\pi}{3R_0}$,
where m and n are integer numbers and R_0 is the radius of the plasmapause. The values of k_y and k_z, m and n are adjustable parameters in the numerical program and R_0 has changed depending on the particular profile considered. All the data points used are from the SAMNET and IMAGE magnetometer arrays in Northern Europe [9].

3.4.1 Profile 1

The first profile considered is from the geomagnetic storm of Halloween 2003. This event was an extreme storm event. The storm took place on 29 October 2003. The steep plasmapause density gradient occurred on 1 November, following plasmaspheric erosion. The data used is for one density profile from the morning sector. Data values are listed in table 3.1;

L	Mass density[amu/cc]
2.39	1415.732
2.79	781.877
3.15	385.849
3.32	287.000
3.60	238.690
3.84	290.703
5.10	80.959

Table 3.1: Data of Halloween 2003

Analytic Fit of the Density Profile

The data of table 3.1 are matched with the following set of parameters appearing in equations 3.35, 3.36 and 3.34.
$N_{in} = 1415.732$, $x_{in} = 2.39$, for ρ_{in}
$N_{out} = 80.959$, $x_{out} = 5.10$, for ρ_{out}
$R_0 = 3.1$,
and
$\delta = 0.2$.
In these expressions, ρ_{in} is the density inside the plasmasphere, ρ_{out} is the density outside, R_0 is the position of the plasmapause and δ is the transition length over which a sharp density decline is observed. These values are set so as to provide a good fit of the data in table 3.1. The unit of density amu/cc. Figure 3.5 shows a fit of the data in table 3.1 together with the analytic fit. The small structure in the density profile seen at $L \sim 3.6$ is due plasma irregularities at the plasmapause boundary layer, which is another area of research [35], and is out of the scope of this thesis. Therefore this structure is ignored in the analytic fit of the density profile. The corresponding Alfvén velocity profile is also plotted in figure 3.6 for the same density profile.

Calculation of the Q factor and trapped modes:

Following the numerical method explained in section 3.3 the discrete values of complex frequencies are calculated for various values of k_y and k_z. For the parameters $m = 0$, and $n = 5$ the result for the imaginary part of the frequency, ω_i and the corresponding Q values are plotted as a function of the real frequency, ω_r, in figure 3.7 The frequency range considered is between 0.01 Hz and 0.5 Hz. All the frequency values in this section and in the following sections are in the units of hertz. The L value, distance from the

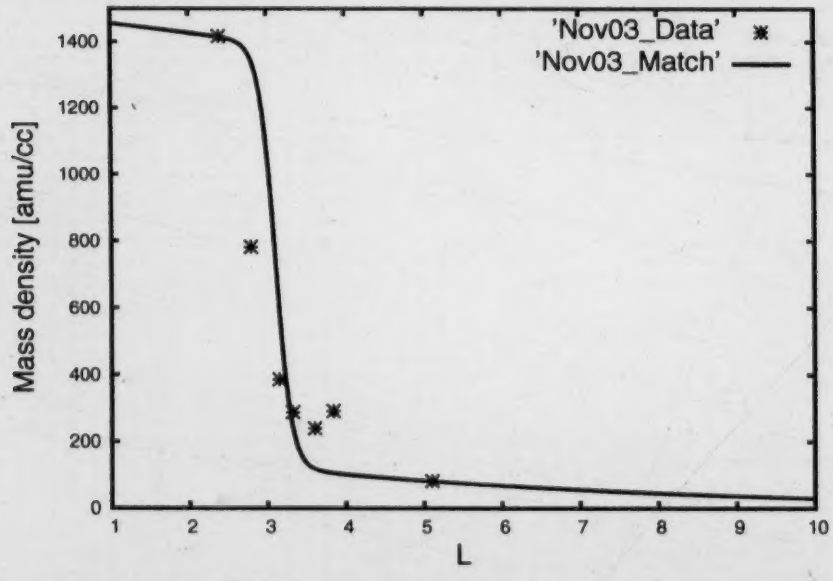

Figure 3.5: 1 November 2003 density data and the fitted profile with equation 3.33 with $N_{in} = 1415.732$, $x_{in} = 2.39$ for ρ_{in} and $N_{out} = 80.959$, $x_{out} = 5.10$ for ρ_{out}, $R_0 = 3.1$ and $\delta = 0.2$. The stars show the measured data and the line shows the fitted profile.

Earth, ranges between $1 - 25$. $L_{max} = 25$ is chosen to be far enough from Earth so that the WKB approximation is applicable.

With m set to 0, equivalently $k_y = 0$, the Alfvén and compressional modes are decoupled. That is equations 3.19 and 3.20 could be written as two separate equation and solved independently. The total energy density and effective potential function are calculated for the frequencies of the high Q values in the bump region. It is found that as long as the frequency values in the bump region are chosen, confining potentials and a good localization in the total energy densities are observed thus demonstrating the quasi-trapped modes in the plasmapause. Whereas, farther away from the bump region, none of the values provided a confining potential graph or localization in the energy density graph. An example of potential graph and energy localization corresponding to a high Q factor value of the bump region are shown in figure 3.8. The range of frequency where of quasi-trapped modes are obtained is from $\omega_r = 0.283$ Hz, $\omega_i = -1.450 \times 10^{-3}$ Hz to $\omega_r = 0.351$ Hz, $\omega_i = -1.500 \times 10^{-3}$ Hz. Outside this range trapped modes are not present anymore. Anywhere outside the bump region and surrounding frequency

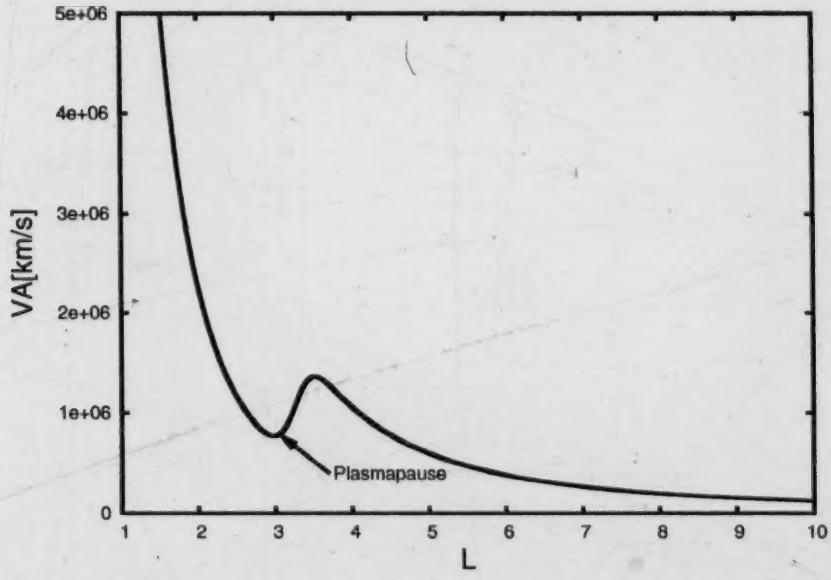

Figure 3.6: Alfvén velocity profile for the data of 01 November 2003.

values, no interesting features are found in the effective potential or in the total energy density. Figure 3.9 shows the total energy as a function of L for a low Q value frequency, $\omega_r = 0.269$ Hz, $\omega_i = -1.44 \times 10^{-3}$ Hz, and $Q = 93.3$. It is also noted that for high Q factor not included in the bump region no significant features are obtained, and the total energy density plot does not show any localization at the plasmapause. Figure 3.10 shows an example of the result found using one of the highest Q frequency value, $\omega_r = 0.365$ Hz, $\omega_i = -1.510 \times 10^{-3}$ Hz, and $Q = 120.8$. For very low frequency values the energy decays before penetrating into the plasmasphere or at the plasmapause, and the effective potential profile is shallow and does not support trapped modes. Figure 3.10 illustrates an example of the results where a value of the frequency corresponding to one of the lowest Q factors is chosen; $\omega_r = 0.101$ Hz, $\omega_i = -1.23 \times 10^{-3}$ Hz, and $Q = 41.1$.

Calculation of coupled modes, $k_y \neq 0$

When the parameter m is set to an integer value other than 0, k_y is not zero anymore and coupled modes are obtained. The graphs of ω_r versus ω_i and Q factor versus ω_r

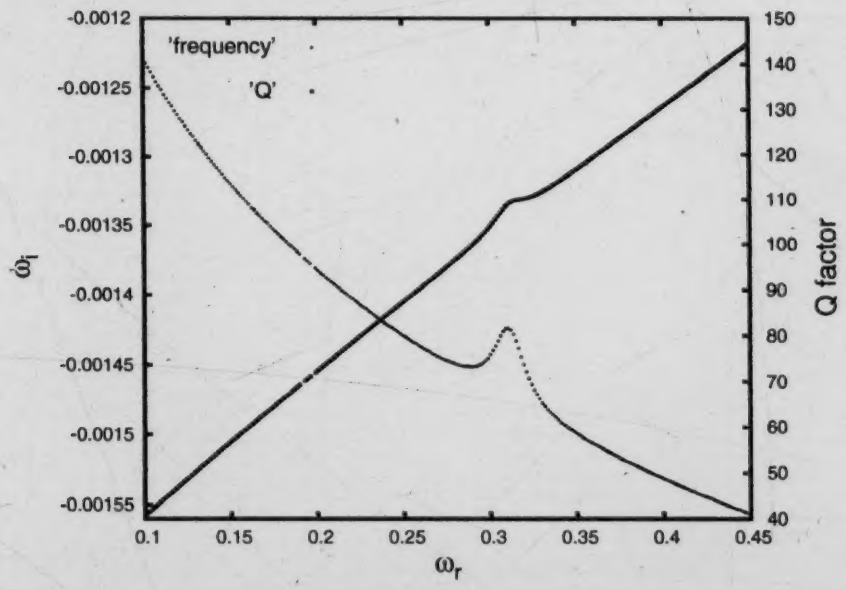

Figure 3.7: Imaginary part of the frequency, ω_i and Q factor as a function of the real part, ω_r for the profile of figure 3.5, with frequencies in units of Hertz. These results are obtained with $m = 0$ and $n = 5$. These values correspond to $k_y = 0$ and $k_z = 5\pi/3R_0$. The interval in L was $1 \leq L \leq 25$, and frequency values are 0.01 to 0.5.

are included in figure 3.11 for $m = 1$ and $n = 5$. The range of frequencies and L are the same as in the calculations of the decoupled modes. The results are similar to the results obtained with the decoupled modes. In particular, there is spatial localization in the total energy density graph and a nice confining potential profile for the frequencies corresponding to Q values of the bump region. These features are not seen for frequencies outside the bump region. The Q factor as a function of real frequency however has a second sharp structure right after the broader bump region (see figure 3.11). There is no localization in the energy density at or around this second peak region, which is caused by coupling between the compressional and the Alfvén modes. There are sharp structures in the graphs of total energy and potential as well, due to coupling of the Alfvén and compressional modes. An example of total energy and corresponding effective potential as a function of L is presented in figure 3.12 for a frequency value corresponding to a Q factor of the broader bump region, the first bump in the graph 3.7. For the coupled modes; the parameters set as $n = 1$ and $m = 5$. A sharp localization in the total energy

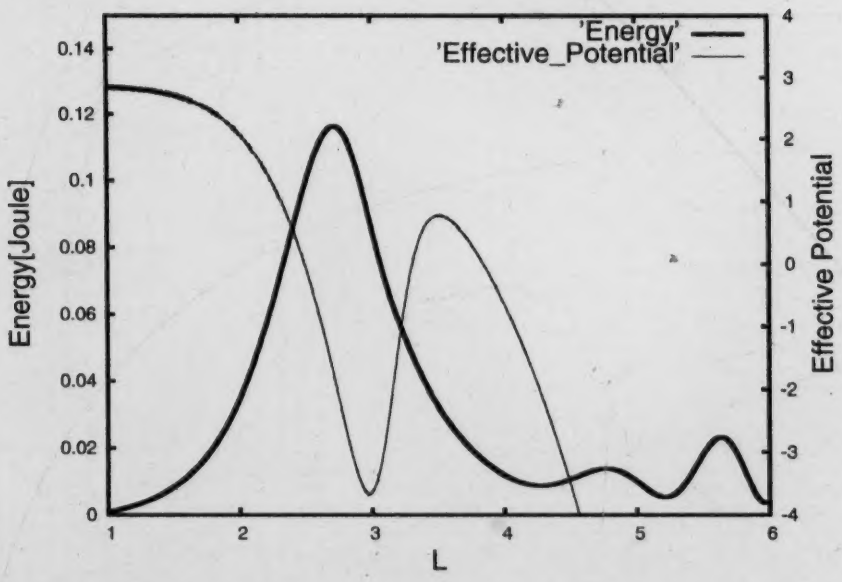

Figure 3.8: Potential function and total energy density as a funtion of L for a frequency corresponding to a high Q factor of bump region for profile 1; $Q = 108.9$, and $\omega_r = 0.310$ Hz

density occurs at the same position as those in the ' potential function graph (see figure 3.12). If the potential funtion is scaled a confining potential well is still observed at the plasmapause, thus causing the trapped modes. Therefore for $k_y > 0$ coupling and trapping at the plasmapause occurs simultaneously. In the case of coupled modes the frequency range where the total energy localization at the plasmapause is observed is from $\omega_r = 0.283$ Hz, $\omega_i = -1.44 \times 10^{-3}$ Hz to $\omega_r = 0.345$ Hz, $\omega_i = -1.42 \times 10^{-3}$. These values of frequency corresponds to the first bump in the Q factor as a function of ω_r graph, as for decoupled modes.

The above results show that trapping is essentially the same for coupled and decoupled modes for a particular type of density profile at the plasmapause. However due to coupling between shear and compressional modes extra features are present in the graphs of effective potential and the total energy as a function of L. Coupling is obtained only if the parameter $m \neq 0$ in which case near singularities are found in the effective potential and the total energy density graphs (see figure 3.12).

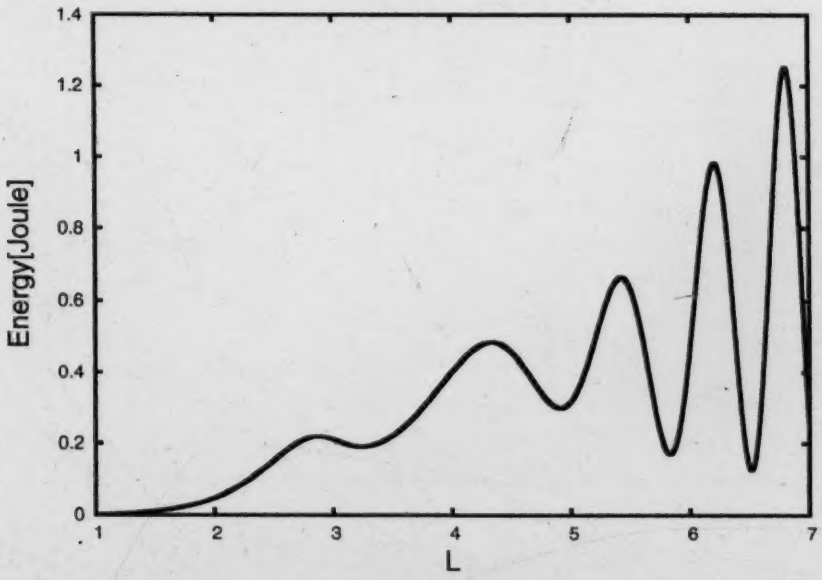

Figure 3.9: Illustration of the energy density as a function of L for one of the frequency values corresponding to a low Q factor of profile 1, for $m = 0$ and $n = 5$. The frequency used for above graph is $\omega_r = 0.269$ Hz, corresponding to $Q = 93.3$ from figure 3.7.

3.4.2 Profile 2

This profile is taken from the event of 14 May 2001. This was a moderate geomagnetic storm of prolonged interval 5-17 May 2001. 14 May 2001 was a particularly interesting day where the second recovery started after renewed geomagnetic activity during the recovery phase of a geomagnetic storm of May 07 2001, described fully in [19]. The data points are provided from the day-side and listed in table 3.2;

Analytic Fit of the Density Profile

Following the same approach as in section 3.4.1 the data of table 3.2 are matched with the following set of the parameters in equation 3.33.
$N_{in} = 2031.472$, $x_{in} = 2.39$ for ρ_{in},
$N_{out} = 52.702$, $x_{out} = 5.35$ for ρ_{out},
$R_0 = 2.92$,

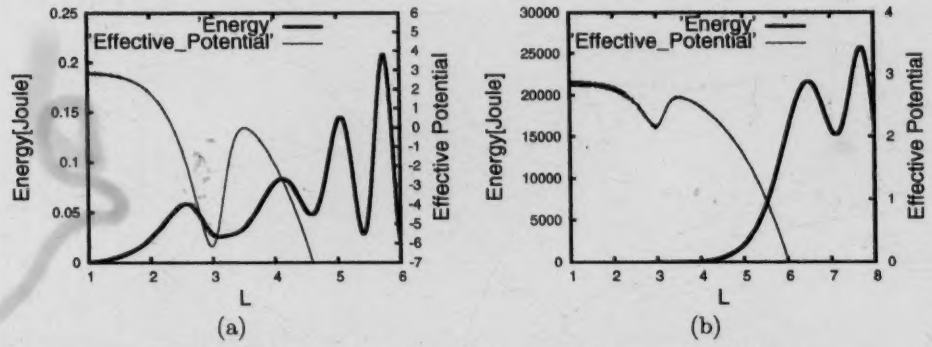

Figure 3.10: Total energy density and corresponding effective potential as a function of L for profile 1, with $m = 0$ and $n = 5$. Figure (a) illustrates the results of a high Q and figure (b) low Q. The frequencies are, $\omega_r = 0.365$ Hz for the higher Q, and $\omega_r = 0.101$ Hz for the lower one. These frequencies correspond to $Q = 120.8$ and $Q = 41.1$ in figure 3.7. It is readily seen from the above graphs that the wave penetrates into the inner plasmasphere and that no trapping is present for the higher frequency and that it decays before reaching to the plasmasphere for the lower one.

and

$\delta = 0.2$.

Figure 3.13 shows a fit of the data in table 3.2 together with the analytical fit. The value of the Alfvén speed is also plotted as a function of L for the profile of figure 3.13 which resulted again with a profile which could support quasi-trapped modes (see figure 3.14).

Calculation of the Q factor and trapped modes:

The Q factor is calculated for profile 2 using the same numerical approach as in section 3.3. The results are similar to the results of profile 1. First decoupled solutions with the set of parameters as $m = 0$, i.e $k_y = m/R_0 = 0$, and $m = 3$, are presented in figure 3.15. The range of L and frequency is the same as with profile 1; L is from 1 to 25 and ω_r is from 0.01 to 0.5 in the units of Hertz. It is worth to note that contrary to what was found with profile 1 with $n = 0$ and $n = 5$, the Q factor and the frequency spectrum does not provide the quasi-trapped modes in the plasmasphere, for profile 2. The important structure of bumps in the graphs are not obtained and correspondingly no trapped modes are obtained. However, the set of parameters $n = 0$ and $m = 3$ provides good results for the current profile, as shown in figure 3.15. The similarities

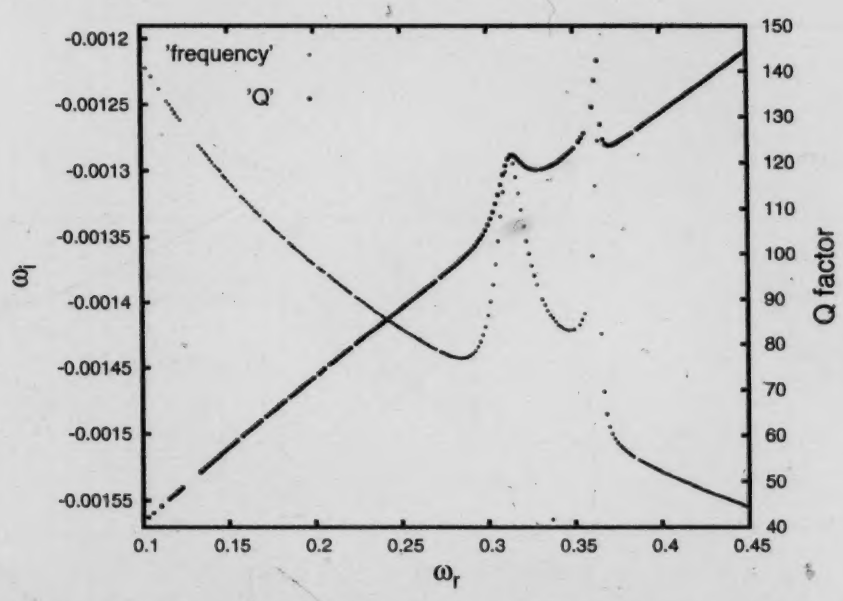

Figure 3.11: Illustration of imaginary frequency, ω_i, and Q factor as a function of ω_r(Hz) for profile 1. The parameters are $m = 1$, $n = 5$ which correspond to coupled modes. A second sharp variation occured in addition to the first one obtained for decoupled modes where $m = 0$. This second sharp structure is due to mode coupling leading to a near singularity.

between figures 3.7 and 3.15 are easily seen, only the frequency range where the sharp structure is seen slightly differs.

The investigation of the quasi-trapped modes of profile 2 is done the same as profile 1. The results of the energy localization region and potential function as a function of L values are also analogous to those found with profile 1. Only the bump region of figure 3.15 produces quasi-trapped modes, and high and low frequency values again give totally penetrating modes and modes that do not tunnel through the plasmapause region respectively. The plasmapause is at $L = 2.92$ for profile 2, corresponding to 14 May 2001 event. Figure 3.16 is included as an example of the result of a frequency value of the bump region. Different results for low and high frequencies are not included since they are also very similar to those included for the profile 1, 14 November 2003 event profile (see figures 3.8 3.9, 3.10). The frequency range where a nice localization in the total energy density is obtained for is, between $\omega_r = 0.229$ Hz, $\omega_i = -1.63 \times 10^{-3}$ Hz,

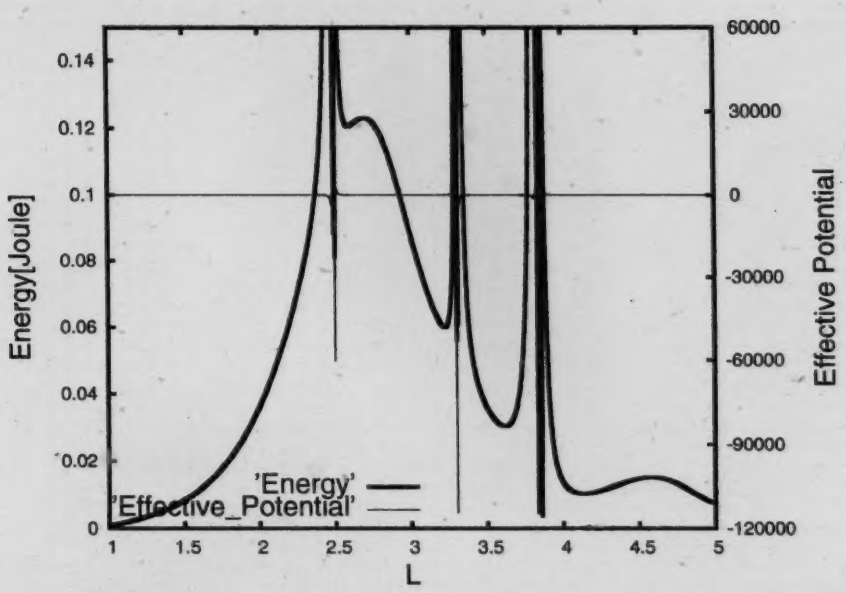

Figure 3.12: Total energy and potential as a function of L for one of the real frequency values corresponding to a high Q factor for $m = 1$ and $n = 5$, of Profile 1. The real frequency value used for the above plots is $\omega_r = 0.313$ Hz, corresponding to $Q = 121.5$ from figure 3.11.

and $\omega_r = 0.260$ Hz, $\omega_i = -1.66 \times 10^{-3}$ Hz which is within the bump region as seen in graph 3.15.

Investigating coupled modes; $k_y \neq 0$

Coupled modes in profile 2 are also investigated, and it is found again that results are similar to those of profile 1. Similar to profile 1, a second sharp structure is observed in the Q factor as a function of ω_r plot (see figure 3.17). This second sharp structure does not provide any significant effect on the effective potential and the total energy density graphs as a function of L. A localization in the total energy density and nice confining effective potential are found around the bump region corresponding to approximately the same region of the decoupled modes. An example of the total energy density as a function of L is included in figure 3.18 for a high Q value frequency in the bump region of figure 3.17. The frequency range where a nice localization of total energy observed for coupled modes is from $\omega_r = 0.205$ Hz, $\omega_i = -1.608 \times 10^{-3}$ Hz, to $\omega_r = 0.274$ Hz ,

L	Mass density[amu/cc]
2.39	2031.472
2.67	1414.097
2.78	1307.400
2.80	1390.533
2.92	1000.504
3.08	625.856
3.16	419.811
3.34	308.049
3.58	158.683
3.60	204.82
3.63	138.483
3.80	97.975
3.90	84.465
3.92	82.817
4.12	89.136
4.76	76.431
4.97	71.342
5.20	56.924
5.35	52.702
5.49	41.343
5.82	40.786
5.89	37.002
6.15	35.199
6.46	51.880
6.54	38.553

Table 3.2: Data of May 2001

$\omega_i = -1.55 \times 10^{-3}$ Hz.

3.4.3 Profile 3

The data of profile 3 was from the event of September 1998. This was an extreme magnetic storm that took place on September 25 . The steep plasmapause density profiles were observed on the 27th and 28th September. Data is provided for the morning sector of September 27th and shown in table 3.3.

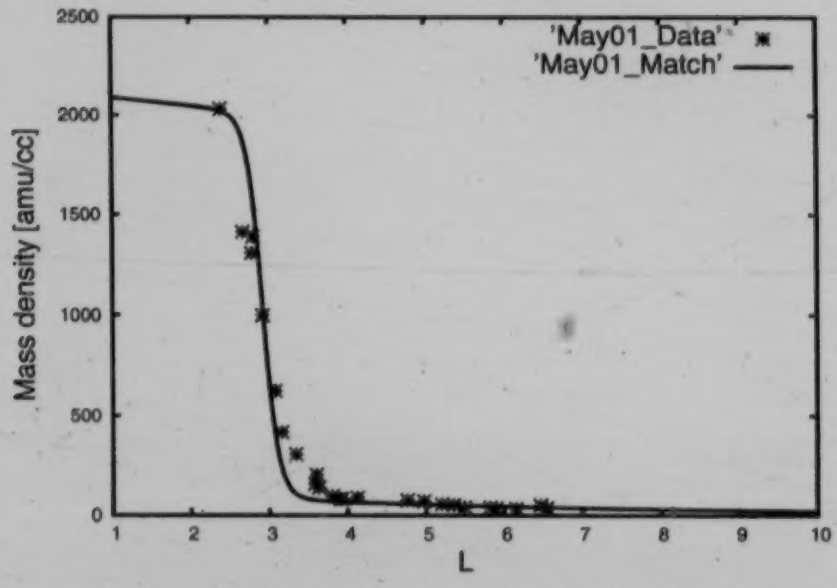

Figure 3.13: Illustration of the density profile for the data of 14 May 2001, table 3.2. The stars show the measured data and the line shows the fit obtained with equation 3.33 computed with $N_{in} = 2031.472$, $x_{in} = 2.39$ for ρ_{in} and $N_{out} = 52.702$, $x_{out} = 5.35$for ρ_{out}, $R_0 = 2.92$ and $\delta = 0.2$.

Analytic Fit of the Density Profile

For the 27 September 1998, the parameters in equation 3.33 are set to;
$N_{in} = 927.39$, $x_{in} = 2.81$ for ρ_{in}
$N_{out} = 18.92$, $x_{out} = 6.12$ for ρ_{out}
$R_0 = 3.56$,
and
$\delta = 0.2$.
The match is shown in figure 3.19, and the Alfvén speed profile is shown in figure 3.20. Similar to what was found with profiles 1 and 2 a profile capable of supporting trapped modes is also found here.

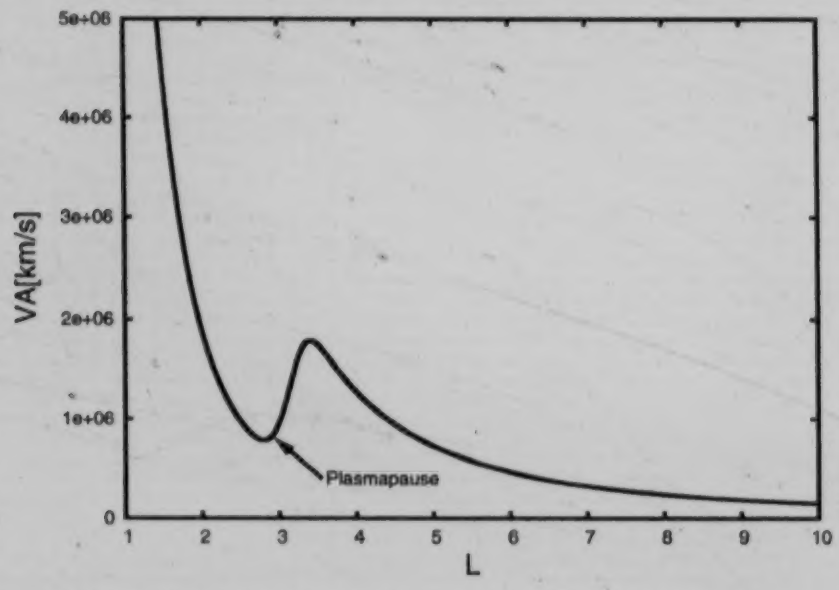

Figure 3.14: Illustration of the Alfvén speed as a function of L for the data of 14 May 2001. It can be seen that the quasi-trapped modes are possible with the above characteristics of the Alfvén speed profile.

Calculation of the Q factor and trapped modes:

The Q factor is calculated for different sets of parameters for profile 3 as well, and again results are similar to those of profiles 1 and 2. For decoupled modes the mode parameters are set to $m = 0$ and $n = 3$ and for the coupled modes they are set to $m = 1$ and $n = 3$. As with profile 2, the set of parameters $n = 0$, $m = 5$ and $n = 1$, $m = 5$ does not lead to mode localization. The frequency spectrum and the Q factor as a function of ω_r are shown in figure 3.21 for decoupled modes and in figure 3.22 for coupled modes. For the coupled modes, a second peak to the right is also obtained as seen in figure 3.22 where energy localization is not present. This is similar to what was obtained with profiles 1 and 2. For energy localization, which is analogous to the results of profiles 1 and 2, two graphs are provided as examples in figures 3.23 and 3.24, for two high Q values within the bump region corresponding to coupled and decoupled modes. The frequency range where a good localization is obtained is from $\omega_r = 0.142$ Hz, $\omega_i = -2.18 \times 10^{-3}$ Hz to $\omega_r = 0.188$ Hz, $\omega_i = -2.307 \times 10^{-3}$ Hz for decoupled modes, and from $\omega_r = 0.142$ Hz,

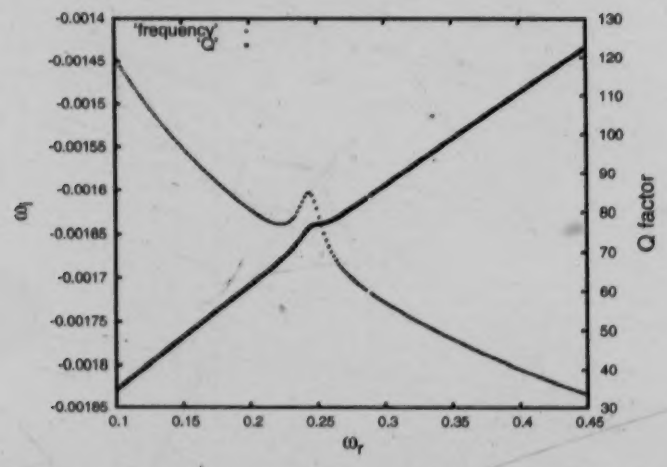

Figure 3.15: Frequency spectrum and Q factor as a function of ω_r(Hz), for Profile 2 (14 May 2001 event), and $n = 0$, and $m = 3$. This corresponds to decoupled modes, $k_y = 0$. Features are found to be quite similar to those of figure 3.7 for profile 1.

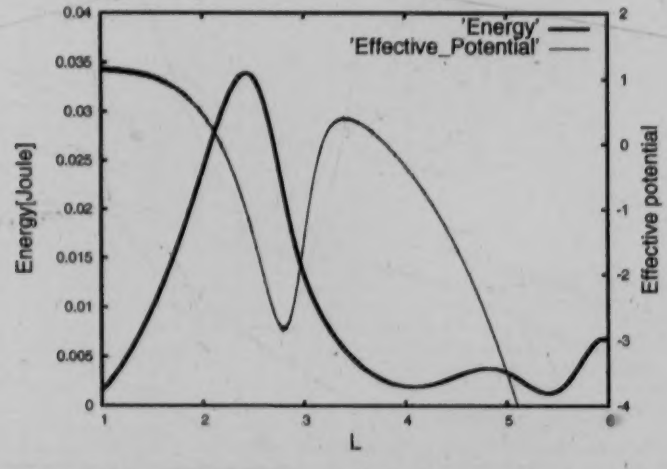

Figure 3.16: Plots of the total energy and effective potential as a function of L for a frequency value corresponding to the local maximum in Q in figure 3.15, for the 14 May 2001 event (profile 2). The frequency for this particular graph is $\omega_r = 0.245$ Hz, corresponding to $Q = 76.5$. The values outside of the local maximum provided neither a nice confining potential nor a localized total energy density similar to the results of profile 1.

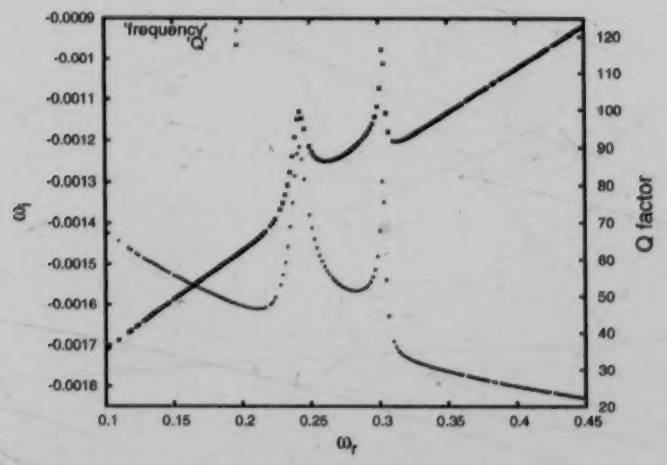

Figure 3.17: ω_i and Q factor as a function of ω_r(in units of Hz) for the coupled modes of profile 2. These curves are obtained with; $m = 1$ and $n = 3$.

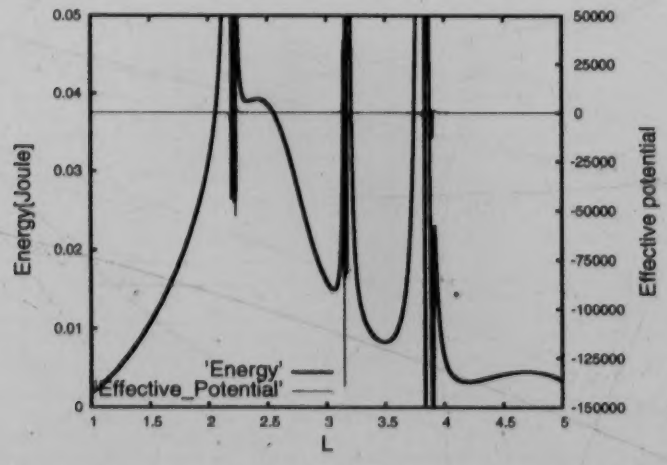

Figure 3.18: Plots of the total energy and effective potential as a function of L for a frequency value corresponding to the peak region of Q in figure 3.17, profile 2. The frequency used for this particular graph is $\omega_r = 0.241$ Hz, corresponding to $Q = 99$. Frequencies outside of this first bump region do not correspond a good localization in the total energy density low mode confinement.

L	Mass density[amu/cc]
2.81	927.39
3.58	402.27
3.79	193.29
4.74	39.66
5.19	35.25
5.33	19.20
5.56	20.07
5.70	35.06
5.73	15.69
6.08	19.25
6.12	18.92
6.44	12.96
6.51	12.32
8.18	12.28

Table 3.3: Data of September 1998

$\omega_i = -2.16 \times 10^{-3}$ Hz to $\omega_r = 0.177$ Hz, $\omega_i = -2.108 \times 10^{-3}$ Hz for coupled modes. The frequency range leading to quasi-trapped modes, and energy density localization, is approximately the same, and it corresponds to the lower frequency peak in the Q factor as a function of L for both coupled and decoupled modes.

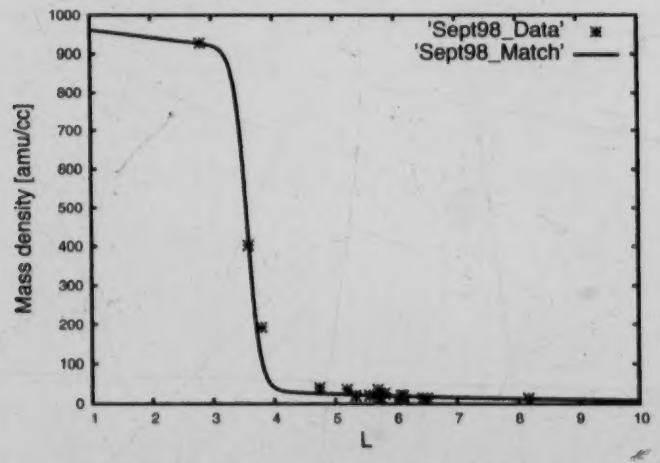

Figure 3.19: Matched density profile for data of the 27 September 1998 given in table 3.2, stars show the actual data and the line shows the fitted profile from equation 3.33 with $N_{in} = 927.39$, $x_{in} = 2.81$ for ρ_{in} and $N_{out} = 18.92$, $x_{out} = 6.12$, for ρ_{out}. Also $R_0 = 3.56$ and $\delta = 0.2$ for this profile.

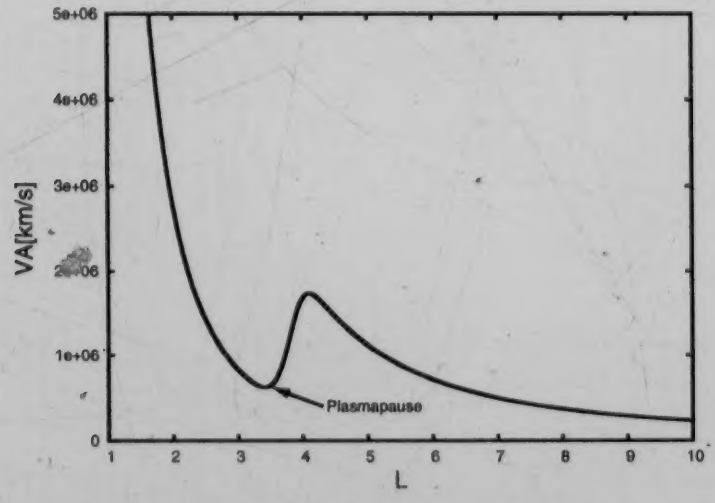

Figure 3.20: Alfvén speed as a function of L for the data of 27 September 1998. The profile suggests here again the possible trapping at the plasmapause.

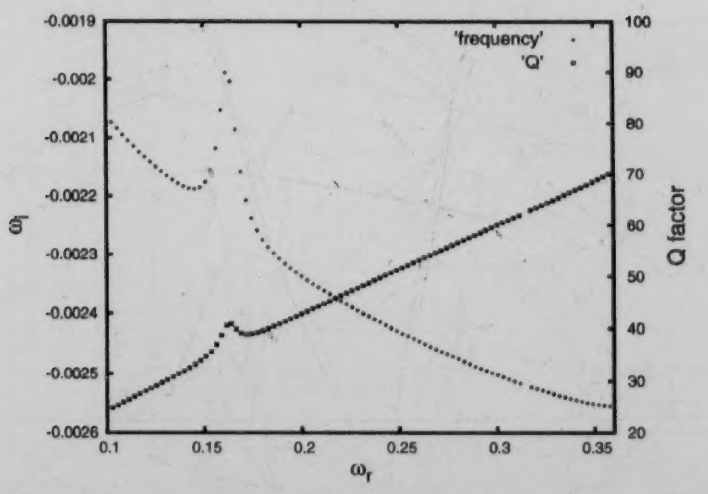

Figure 3.21: Q factor and ω_i as a function of real frequency ω_r(in units of Hz) for the data of 27 September 1998 for $m = 0$ and $n = 3$. It is easily seen that the characteristics are quite similar to those of profiles 1 and 2 (see figures 3.7 and 3.15).

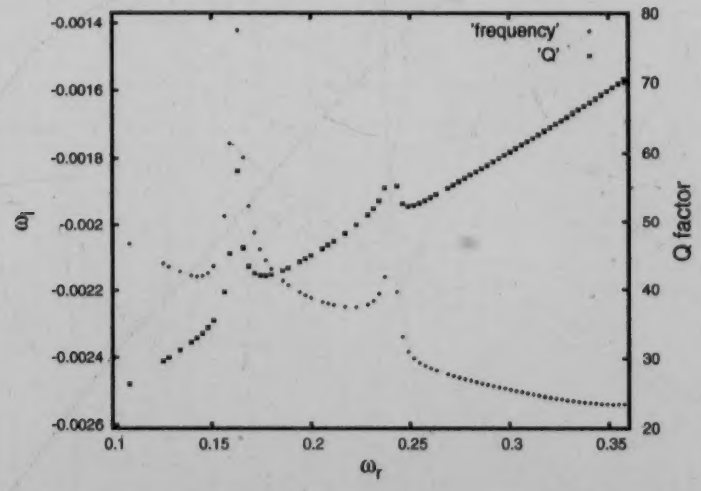

Figure 3.22: Frequency spectrum and Q factor for the coupled modes of profile 3. corresponding to $n = 1$ and $m = 3$. As with the graphs of profile 1 and 2, two bumps are observed in the coupled modes frequency(in units of Hz) and Q factor spectrum for profile 3 (27 September 1998 event).

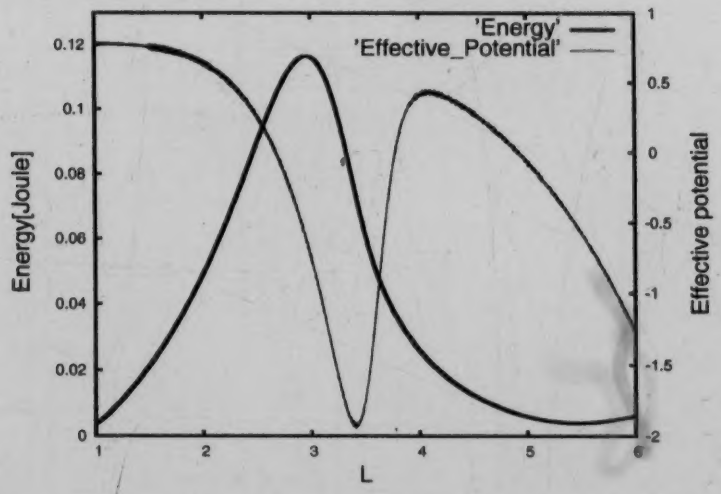

Figure 3.23: Total energy density and effective potential as a function L for $m = 0$, $n = 3$ for the 27 September 1998 event. The frequency is $\omega_r = 0.161$ Hz corresponding to a $Q = 40.56$ of figure 3.21.

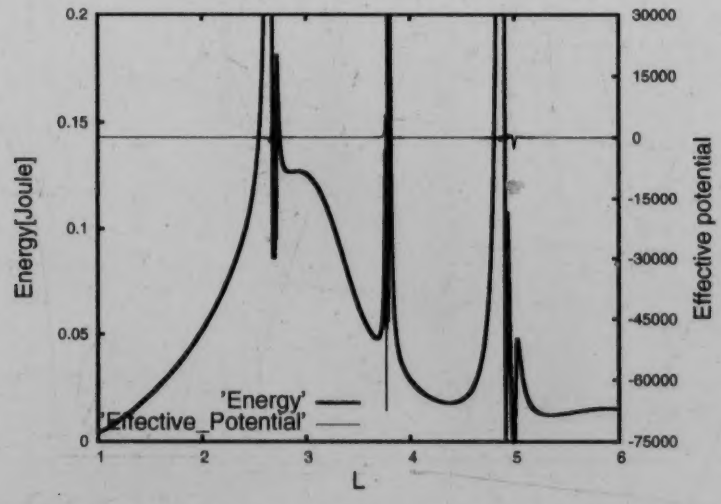

Figure 3.24: Total energy density and effective potential as a function L for $m = 1$, $n = 3$ for the 27 September 1998 event. The frequency used is $\omega_r = 0.163$ Hz corresponding to a $Q = 57.3$ of figure 3.22.

Chapter 4

Conclusion and Future Work

4.1 Concluding Remarks

The results presented in this thesis embody a contribution to the understanding of mode trapping in the plasmapause. This work is based on a numerical approach to demonstrate the possibility of quasi-trapped or trapped modes in the plasmapause due to its particular density profile; a sharp decline especially during and after geomagnetic storms.

Chapter 2 introduces an ideal case for investigating trapping or quasi-trapping in a potential well that is analogous to the potential at the plasmapause. In this chapter the analysis is done using a one dimensional wave equation similar to the Schrödinger equation. A model wave function is derived and trapping is investigated for a continuous spectrum with an incoming wave with unit amplitude. The graph of the maximum amplitude in the well region, as a function of the frequency, shows sharp peaks suggesting trapping. The wave equation is then solved as an eigenvalue problem resulting in a discrete frequency spectrum. This second approach is formulated in terms of a boundary condition that corresponds to an outgoing wave in the region outside the well. The Q factor is calculated and plotted as a function of discrete frequencies. High values of Q are obtained for frequency values that correspond to peaks in amplitude in the previous section. The wave function is plotted as a function of distance using frequency values corresponding to high Q factor and localization is observed in the potential well region suggesting possible trapping. First, the problem is formulated analytically in terms of a set of linear algebraic equations. It is solved using LU decomposition. It is then formulated numerically in terms of a second order ordinary differential equation with prescribed boundary conditions. The comparison between the results obtained with these two approaches is useful for the purpose of testing the validity of the numerical

approach that is used in the more realistic problem of chapter 3. Both appraoches gave perfectly superposing results, proving that the numerical approach used is appropriate.

In chapter 3, quasi-trapped compressional modes in the plasmapause is investigated using a box model of the magnetosphere. The wave equation for compressional modes is derived and solved using a fourth order Runge-Kutta method. The waves are assumed to be initiated in the region of the plasmapause. The velocity wave function is assumed to vanish on the left boundary corresponding to the surface of the Earth. A discrete frequency spectrum is then found using a root finder. From there, the values of the Q factor are calculated for three different density profiles observed during three different geomagnetic storms, the storms of 01 November 2003, 14 May 2001 and 27 September 1998.

The results obtained with these three profiles have similarities in their Q factors, and frequency spectra, the total energy densities and potential functions. For decoupled modes the Q factor as a function of ω_r is characterized by a bump in a certain region of frequency for all three profiles. In this region, localization in the total energy density, in other words quasi-trapped modes, is present. With the coupled shear and compressional modes an extra peak appears in the Q factor and in the frequency spectrum. This is observed for all three profiles considered. However, this peak does not correspond to any special feature; that is, no localization in total energy density is obtained. For the coupled modes, sharp peaks are also seen in the energy and potential function graphs as a function of L besides the localization.

Quasi-trapped modes are obtained for all the profiles with the appropriate set of parameters, that suggest possible trapping in the plasmapause region. The frequency range for which a good energy localization is observed are slightly different for each profile, suggesting a change of frequency range for different density profiles of the plasmapause.

Overall, this thesis has shown that trapping of compressional modes is possible in the plasmapause due to Alfvén velocity valley associated with the sharp density gradient occurs after geomagnetic storms, and the frequency range where trapping is observed depends on the density profile considered.

4.2 Future Work

Future work may include a thorough investigation of the coupled modes of the three profiles. The extra peak in the Q factor as a function of real the frequency is not fully understood, thus more work on the coupled modes could possibly be useful to understand this feature. Also the same analysis could be done on different density profiles of the

plasmapause. Moreover trapped modes in the plasmasphere could be further investigated as a possible cause for the low latitude ULF pulsations.

More realistic results could be observed if a better magnetospheric model is used such as a dipole model. A more advanced approach could be to look at the problem in two and three dimensions.

Bibliography

[1] Allan, W., Menk,F.W., Fraser,B.J., Li,Y., & White, S.P., Are low-latitude Pi2 pulsations cavity/waveguide modes?, *Geophys. Res. Lett.*, Vol:**23**, pg 765-768, 1996

[2] Lee, D-H. Dynamics of MHD wave propagation in the low-latitude magnetosphere, *Jour. of Geophys. Res.*, Vol:**101**, pg 15371-15386, 1996

[3] Lee, D-H., & Kim, K., Compressional MHD waves in the magnetosphere: A new approach, *Jour. of Geophys.Res*, Vol:**104**, pg 12379-12385, 1999

[4] Lee, D-H., Hudson, M.K., Kim, K., Lysak, L.R., & Song, Y., Compressional MHD wave transport in the magnetosphere 1 Reflection and transmission across the plasmapause, *Jour.of Geophys. Res* Vol:**107**,NO.A01, pg 1307, 2002

[5] Baumjohann, W., & Treumann, R.A., Basic Space Plasma Physics, *Imperial Collage Press*, pg 5-10 and 80-85, 1997

[6] Spacojević, M. Global Dynamics fo the Earth's Plasmasphere, *Standford University*, 2003

[7] Kivelson, M.G., &Russel, C.T., Introduction to Space Physics, *Cambridge University Press*, pg 290-300, 1995

[8] Lemaire, J.F., & Gringuaz, K.I., The Earth's Plasmasphere, *Cambridge University Press*, pg 14, 96-105, and 270-275, 2005

[9] Dent, Z.C., Mann, I.R., Golstain, J., Menk, F.W., & Ozeke, L.G., Plasmaspheric depletion, refilling, and plasmapause dynamics: A coordinated ground-based and IMAGE satellite study, *Jour.of Geophys. Res.*, Vol:**111**, A03205, doi:10.1029/2005JA011046, 2006

[10] Elphic, R.C., Weiss, L.A., Thomsen, M.F., & McComas, D.J., Evolution of plasmaspheric ions at geosynchromous orbit during times of high geomagnetic activity, *Geophhys. Res. Lett.*, Vol:**23**, pg 2189-2192, 1996

[11] Spasojević, M., Goldstein, J., Carpenter, D.L., Inan, U.S., Sandel, B.R., Moldwin, M.B., &Reinisch, B.W., Global response of the plasmasphere to a geomagnetic disturbance, *Jour. of Geophys. Res.*, Vol:**108**, NO.A9, pg 1340, doi:10.1029/2003JA009987, 2003

[12] Parks, G.K., Physics of Space Plasmas, *Westview Press*, pg 90-97, 2004

[13] Wolf, R.A., Spiro, R.W., Sazykin, S., & Toffoletto, F.R., How the Earth's inner magnetosphere works: An evolving picture, *Jour. of Atm. and Solar-Terr. Phys.*, Vol:**69**, pg 288-302, 2007

[14] *http://pluto.space.swri.edu/IMAGE/glossary/plasmasphere2.htm*, Oct, 01, 2007

[15] Zarka, P., Planetary magnetospheric structure, *Observatoire de Paris - CNRS, LESIA*, 2006

[16] Carpenter, D.I., Lemaire, J., Erosion and recovery fo the plasmasphere in the plasmapause region, *Space Sci. Rew.*, Vol:**80**, pg 153-179, 1997

[17] Fraser, B.J., Horwitz, J.L., Slavin, J.A., Dent, Z.C., & Mann, I.R., Heavy ion mass loading of the geomagnetic field near the plasmapause and ULF wave implications, *Geophys. Res.Lett.*, Vol:**32**, L04102, doi:10.1029/2004GL021315, 2005

[18] Lemaire, J., Steady state plasmapause positions deduced from McIlwain's electric field models *Jour. of Atm. and Terr. Phys.*, Vol:**36**, pg 1041-1046, 1976

[19] Dent, Z.C., Mann, I.R., Waters, C.L., Golstein, J., Menk, F.W., & Ozeke, L.G., Ground-Magnetometer observation of a cross-phase reversal at a steep plasmapause, *Jour. of Geophys. Res.*, doi:10.1029, 2007

[20] Klimushkin, D.Yu., Resonators for the hydromagnetic waves in the magnetosphere, *Jour. of Geophys. Res.*, vol:**103**, pr 2369-2375, 1998

[21] Molchanov, O.A., Sharko, I.E., Electrostatic ion-cyclotron waves near the plasmapause in the Earth's magnetosphere, *Ins. for Terr. Magn., the Ion., and the Prop. Rad. Waves.*, translated from *Izv. Vyss. Uch. Zav., Radiofizika*, Vol:**25**, pg 263-268, 1982

[22] Sibeck, D.G., Pressure pulses and cavity mode resonances, *Kluwer Acad. Publ*, pg 95-110, Nerherland, 2004

[23] Chen, L., &Hasegawa, A., A theory of long-period magnetic pulsations 2. Impulse excitation of surface eigenmode, *Jour. of Geophys. Res.*, Vol:**79**, No.7, pg 1033-1037, 1974

[24] Lanzerotti, L.J., Mellen, D.B., & Fukunish, H. Excitation of plasma density gradients in the magnetosphere at ultra-low frequencies, *Jour. of Geophys. Res.*, Vol:**80**, No.22, pg 3131-3140, 1975

[25] Morgan, D.D, & Gurnett, D.A., The source location and beaming of terrestrial continuum radiation, *Jour. of Geophy. Res.*, Vol:**96**, No:A6, pg 9595-9613, 1991

[26] Kurth, W.S., Gurnett, D.A., & Anderson, R.R., Escaping non-thermal continuum radiation, Jour. of Geophys. Res, Vol:**86**, No.A7, pg 5519-5531, 1981

[27] Kurth, W.S., & Gurnett, D.A., Plasma waves in planetary magnetospheres, Jour. of Geophys. Res., Vol:**96**, pg 18977-18991, 1991

[28] Yeoman, T.K., & Orr, D., Phase and spectral power of mid-latitude P_i2 pulsations:Evidence for a plasmaspheric cavity resonance, *Planet Space Sci.*, Vol:**37**, No.11, pg 1367-1383, 1989

[29] Xiaoming, Z., & Kivelson, M.G., Global mode ULF pulsations in a magnetosphere with a non-monotonic Alfvén speed, *Jour. of Geophys. Res.*, Vol:**94**, No.A2, pg 1479-1485, 1989

[30] Sutcliffe, P.R., The association of harmonic in P_i2 power spectra with the plasmapause, *Planet Space Sci.*, Vol:**23**, pg 1581-1587, 1975

[31] Kepko, L., & Spence, H.E., Observations of discrete, global magnetospheric oscillations directly driven by the solar wind density variations, *Jour. of Geophys. Res.*, Vol:**108**, No.A6, 1257, doi:10.1029/2002JA009676, 2003

[32] Kepko, L. Spence, & H.E., ULF waves in the solar wind as direct drivers of magnetospheric pulsations, *Geophys. Res. Lett.*, Vol:**29**, No.8, 1197, 10.1029/2001GL14405, 2002

[33] Press, W.H., Teukolsky, S.A., Vetterling, W.T., Flannery, B.P., Metcalf, M., Numerical recipes in Fortran90, Vol:**2**, pg 37,1017, 2002

[34] *http://spaceweather.com/glossary/kp.html*, Dec., 14, 2007

[35] Décréau, P.M.E., Le Guirriec, E., Rauch, J.L., Trotignon, J.G., Canu, P., Darrouzet, F., Lemaire, J., Masson, A., Sedgemore, F., & Adnré, M., Density irregularities in the plasmasphere boundary layer boundary layer: Cluster observations in the dusk sector, *Adv. in Space Phys.*, Vol:**36**, pg 1964-1969, 2005

[36] Lemaire, J. Plasma distribution models in a rotating magnetic dipole and refilling of plasmaspheric flux tubes, *Phys. Fluids B*, Vol:**1**, No:7, pg 1519-1525, 1989